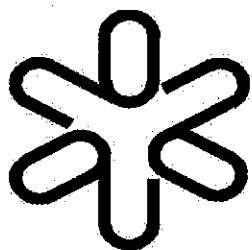


SBI/IFUSP
BASE: 04
SYS Nº: 1080771



Instituto de Física
Universidade de São Paulo

**Experimental determination of the ion-ion potential
in the N=50 target region: a tool to probe ground-
state nuclear densities**

Alvares, M.A.G.; Chamon, L.C.; Pereira, D.; Rossi Jr., E.S.;
Silva, C.P. and Gasques, L.R.

*Laboratório Pelletron, Instituto de Física da Universidade de São Paulo,
São Paulo, Brasil*

Dias, H.

*Grupo de Física Nuclear Teórica e Fenomenologia de Partículas
Elementares, Instituto de Física da Universidade de São Paulo, São Paulo,
Brasil*

Roos, M.O.

*Departamento de Física, Universidade Federal de Mato Grosso, Cuiabá,
Brasil*

Publicação IF - 1355/99

Experimental determination of the ion-ion potential in the N=50 target region: a tool to probe ground-state nuclear densities.

M. A. G. Alvarez, L. C. Chamon, D. Pereira, E. S. Rossi Jr. , C. P. Silva and L. R. Gasques

*Laboratório Pelletron, Instituto de Física da Universidade de São Paulo,
Caixa Postal 66318, 05315-970, São Paulo, SP, Brasil.*

H. Dias

*Grupo de Física Nuclear Teórica e Fenomenologia de Partículas Elementares,
Instituto de Física da Universidade de São Paulo,
Caixa Postal 66318, 05315-970, São Paulo, SP, Brasil.*

M. O. Roos

*Departamento de Física, Universidade Federal de Mato Grosso,
Av. Fernando Corrêa, 78060-900, Cuiabá, MT, Brasil.*

March 16, 1999

Abstract

Precise elastic and inelastic differential cross sections have been measured for the $^{16}\text{O} + ^{88}\text{Sr}, ^{90,92}\text{Zr}, ^{92}\text{Mo}$ systems at sub-barrier energies. From a coupled channel data analysis, the corresponding "experimental" bare potentials have been determined. The comparison of these potentials with those derived from double-folding theoretical calculations and the high energy (96 MeV/nucleon) elastic scattering data analysis indicate that the method is a very sensitive probe of the ground-state nuclear densities in the surface region.

NUCLEAR REACTIONS: $^{88}\text{Sr}(^{16}\text{O}, ^{16}\text{O})^{88}\text{Sr}$, $^{90,92}\text{Zr}(^{16}\text{O}, ^{16}\text{O})^{90,92}\text{Zr}$, $^{92}\text{Mo}(^{16}\text{O}, ^{16}\text{O})^{92}\text{Mo}$, measured elastic and inelastic (2^+) cross sections at $43 \leq E_{\text{LAB}} \leq 49 \text{ MeV}$. Deduced optical potentials. Shell model and double-folding calculations.

I. Introduction

In this work, we present precise elastic and inelastic (2_1^+) differential cross sections for the $^{16}\text{O} + ^{88}\text{Sr}, ^{90,92}\text{Zr}, ^{92}\text{Mo}$ systems at sub-barrier energies, $43 \leq E_{LAB} \leq 49 \text{ MeV}$. The main purpose of the experiment was to determine the bare ion-ion potentials for these systems through coupled channel (CC) elastic and inelastic data analyses. Recently, this method has been successfully applied in a study of the $^{16}\text{O} + ^{58,60,62,64}\text{Ni}$ systems [1, 2]. As discussed in these previous works, it was possible to study the isotopic dependence of the ion-ion potential for the proton closed shell nuclei ($Z=28$), because the coupled channel data analyses at sub-barrier energies are very reliable due to the small number of open reaction channels. In the present work, we investigate the isotonic (Z) dependence of the potential for the neutron closed shell targets ($N=50$) ^{88}Sr , ^{90}Zr and ^{92}Mo , and the influence on the potential due to the two extra neutrons in the ^{92}Zr nucleus.

In the data analysis, the best fits have been achieved with reasonable Coulomb and nuclear phonon amplitudes, and the slopes and strengths of the ion-ion potentials have been determined within 5% accuracy. Through the comparison of the “experimental” (i.e. extracted from data analyses) potentials with those derived from M3Y double-folding calculations, it was possible to probe the ground-state nuclear densities in the surface region ($\rho \simeq 0.01 \text{ fm}^{-3}$). The consistency of these studies has been tested, for the $^{16}\text{O} + ^{90}\text{Zr}$ system, through the comparison of the sub-barrier elastic data analysis with that at much higher energy ($E_{LAB} = 1503 \text{ MeV}$), in which an inner region of the nuclear density is probed. In the optical model high energy data analysis, the non-local exchange effects were taken into account.

The paper is organized as follows: section 2 gives the experimental details and results. The CC data analysis is presented in section 3. In section 4, we study the influence on the potentials due to the increasing number of protons in the $^{16}\text{O} + ^{88}\text{Sr}, ^{90}\text{Zr}, ^{92}\text{Mo}$ systems, and also the influence of the two extra neutrons in the $^{16}\text{O} + ^{92}\text{Zr}$ system. In section 5, we discuss the role played by the reaction channels with negligible cross sections in the polarization potential. In section 6, the sensitivity of our method as a probe of the nuclear densities is discussed. Section 7 contains a brief summary and the main conclusions.

II. Experimental Details and Results

The measurements were made using the ^{16}O beam from the São Paulo 8UD Pelletron Accelerator. The detecting system has been already described in ref. [1]; it consisted of a set of nine surface barrier detectors spaced 5° apart. The thickness of the carbon ($10 \mu\text{g}/\text{cm}^2$) backed ^{88}Sr , ^{90}Zr , ^{92}Zr , ^{92}Mo targets were about $40 \mu\text{g}/\text{cm}^2$, with a layer of gold ($50 \mu\text{g}/\text{cm}^2$) for the purpose of data normalization. We have estimated the Coulomb barrier for the $^{16}\text{O} + ^{88}\text{Sr}$, $^{90,92}\text{Zr}$, ^{92}Mo systems as $V_B^{Lab} \simeq 51, 53, 53$ and 55 MeV , respectively. Data were taken in the bombarding energy range $43 \leq E_{LAB} \leq 49 \text{ MeV}$, which corresponds to 5 to 8 MeV below the Coulomb barrier for these systems. Due to the high precision required for the experimental data, the following procedures were taken into account in the data acquisition and reduction: i) the use of two monitor detectors ($\theta_{LAB} = \pm 35^\circ$) to be sure that no target deterioration occurred during bombardment; ii) high energy resolution to allow (see Fig. 1) a complete separation among the elastic, inelastic (2_1^+) and also the contaminant associated peaks; iii) corrections in the counting rate related to the elastic and inelastic processes due to the small background near those peaks.

Figs. 2 to 7 exhibit the elastic and inelastic (target - 2_1^+) differential cross sections for the $^{16}\text{O} + ^{88}\text{Sr}$, $^{90,92}\text{Zr}$, ^{92}Mo systems. Due to the very small counts in the peaks related to the inelastic process, the corresponding cross sections are somewhat "contaminated" due to the background subtraction, and it was not possible to obtain inelastic cross sections for the $^{16}\text{O} + ^{88}\text{Sr}$, ^{92}Zr systems. No evidence was found in the energy spectra for population of other excited target or projectile states with cross sections near those for the 2_1^+ state. The integrated inelastic cross sections vary between 5 to 50 mb in the energy range investigated. These values are one or two orders of magnitude larger than those associated to other reaction channels, such as the sub-barrier few nucleon transfer [3] and fusion [4] processes.

III. Data Analysis

In the coupled channel calculations, we have adopted a procedure similar to that described in the analysis of the sub-barrier elastic and inelastic data

for the $^{16}\text{O} + ^{58,60,62,64}\text{Ni}$ systems [1, 2]. The target nuclei have been assumed spherically symmetric but susceptible to vibrations around their spherical shapes [5]. For these nuclei, we have considered the contribution of the 2_1^+ state. We have used phonon amplitudes according to Refs. [6, 7, 8]. The value $r_c = 1.06 \text{ fm}$, obtained from electron scattering experiments [9], have been assumed for the Coulomb radius. For the real nuclear potential we have assumed a Woods-Saxon shape with a radius parameter equal to the Coulomb radius ($r_0 = r_c = 1.06 \text{ fm}$). We have used in the CC calculations an inner imaginary potential [1, 2], which takes into account the small internal absorption from barrier penetration. No sensitivity in the CC cross section predictions has been detected related to strength variations of this absorptive potential. The depth, V_0 , and the diffuseness, a , of the real nuclear potential were searched for the best data fits. In a similar way as reported for the $^{16}\text{O} + ^{58,60,62,64}\text{Ni}$ systems [1, 2], for each system and bombarding energy we have found a family of real potentials, with different diffuseness parameters, which give equivalent data fits, as illustrated in Fig. 8 for the $^{16}\text{O} + ^{90}\text{Zr}$ system at the energies of 46 and 48 MeV . These potentials cross (see Fig. 8) at a particular radius, R_S , which is usually referred as the strong absorption radius in the case of higher energy elastic scattering data analysis. At sub-barrier energies, this radius is related to the classical turning point, and is energy dependent. Due to the small absorption involved in this case, in this work we refer to R_S as the sensitivity radius.

We have used the energy dependence of R_S (see Fig. 9) to characterize the shape of the real nuclear potential in the surface region. The uncertainties of the nuclear potential strengths at the sensitivity radius were obtained as already discussed in Refs. [1, 2]. The shape of the nuclear potential is quite close to an exponential, represented by solid lines in Fig. 9. Table 1 gives the diffuseness values obtained for the $^{16}\text{O} + ^{88}\text{Sr}, ^{90,92}\text{Zr}, ^{92}\text{Mo}$ systems. Within the uncertainties, the diffuseness parameters are compatible with the average value $\bar{a} = 0.64 \pm 0.02 \text{ fm}$. This diffuseness value is in good agreement with theoretical double-folding calculations, as will be discussed in the next section. Using the value $a = 0.64 \text{ fm}$ for the $^{16}\text{O} + ^{88}\text{Sr}, ^{90,92}\text{Zr}, ^{92}\text{Mo}$ systems, we were able to fit all the angular distributions (see Figs. 2 to 7) with an energy-independent bare potential for each system. Table 1 gives the CC potential strengths for all the systems investigated in this work at the interaction radius $R = 11 \text{ fm}$, which is near the center of the sensitivity region.

IV. Double-Folding Calculations

In this section, we present the theoretical calculations with the aim of evaluating the nuclear ion-ion potential by using the double-folding method [10] with shell model densities. In such analyses, we have used the well known nucleon-nucleon M3Y interaction in its standard form [10].

$$v_o(r) = \left[7999 \frac{e^{-4r}}{4r} - 2134 \frac{e^{-2.5r}}{2.5r} \right] + 262 \delta(\vec{r}) \text{ MeV} \quad (1)$$

In our calculations, the ground-state density of the ^{16}O nucleus was derived from electron scattering experimental results [9], with the assumption that the neutron (ρ_n) and proton (ρ_p) densities have the same shape as the charge density (ρ_c). The total nuclear density is expressed by:

$$\rho(r) = \rho_n(r) + \rho_p(r) = \rho_0 \left[1 + \gamma \left(\frac{r}{c} \right)^2 \right] e^{-\left(\frac{r}{c} \right)^2}, \quad (2)$$

where $\gamma = 1.544$, $c = 1.833 \text{ fm}$ (charge density parameters of Ref. [9]), and $\rho_0 = 0.1407$ to satisfy the normalization condition:

$$\int_0^\infty 4\pi\rho(r)r^2 dr = N + Z = A. \quad (3)$$

For the target nuclei we have used densities from shell model calculations, assuming, for the ^{88}Sr , ^{90}Zr and ^{92}Mo nuclei, the $N = 50$ neutron closed shell and the $(2p_{3/2}, 1f_{7/2}, 2p_{1/2}, 1g_{9/2})^{Z-28}$ proton orbital configuration. For the ^{92}Zr nucleus, we have considered the $(1f_{7/2}, 1f_{5/2}, 2p_{3/2})^{18} (2p_{1/2}, 1g_{9/2})^2$ proton and the $(1g_{9/2})^{10} (1g_{7/2}, 2d_{5/2}, 2d_{3/2}, 3s_{1/2})^2$ neutron orbital configurations. The shell model calculations predict level schemes for these nuclei which are in reasonable agreement with those derived from experiments up to excitation energies of about 3 MeV (see Fig. 10).

Fig. 11 presents the proton (dashed lines) and neutron (solid lines) densities for the ^{88}Sr , $^{90,92}\text{Zr}$ and ^{92}Mo nuclei. For these nuclei, the number of protons is significantly smaller than the number of neutrons, thus the proton densities are somewhat more internal as compared to the corresponding

neutron ones. We have calculated the folding potential contributions of the proton and neutron target densities according to the following expressions:

$$V_p(R) = \int \rho_o(\vec{r}_1) v_o(|\vec{R} - \vec{r}_1 + \vec{r}_2|) \rho_p(\vec{r}_2) d\vec{r}_1 d\vec{r}_2, \quad (4)$$

$$V_n(R) = \int \rho_o(\vec{r}_1) v_o(|\vec{R} - \vec{r}_1 + \vec{r}_2|) \rho_n(\vec{r}_2) d\vec{r}_1 d\vec{r}_2, \quad (5)$$

$$V_T(R) = V_p(R) + V_n(R) = \int \rho_o(\vec{r}_1) v_o(|\vec{R} - \vec{r}_1 + \vec{r}_2|) \rho_T(\vec{r}_2) d\vec{r}_1 d\vec{r}_2, \quad (6)$$

where ρ_o is the total ^{16}O density; ρ_p , ρ_n and ρ_T are the proton, neutron and total target densities, respectively; and V_p , V_n and V_T are the corresponding proton, neutron and total folding potentials. These folding potentials are shown in Fig. 12. As expected, due to the neutron and proton density features (see Fig. 11), the neutron potential contribution in the surface interaction region is significantly more important in comparison to the corresponding proton one.

Since the neutron densities for the ($N = 50$ closed shell) ^{88}Sr , ^{90}Zr and ^{92}Mo nuclei are quite similar in the surface density region (see Fig. 13), the corresponding $^{16}\text{O} + ^{88}\text{Sr}$, ^{90}Zr , ^{92}Mo systems present, as expected, similar double-folding potentials for large interaction distances (see Fig. 14 bottom). The neutron density for the two extra neutron ^{92}Zr nucleus, as indicated in Fig. 13, is shifted by about 0.1 fm in the surface region in relation to the other target nuclei. Since this value is of the same order of magnitude of the potential diffuseness ($a \simeq 0.6 \text{ fm}$), the double-folding theoretical calculations predict for the $^{16}\text{O} + ^{92}\text{Zr}$ system a bare potential which is about 20% greater in the surface region as compared to those for the $^{16}\text{O} + ^{88}\text{Sr}$, ^{90}Zr , ^{92}Mo systems (see Fig. 14). We point out that the $^{16}\text{O} + ^{92}\text{Zr}$, ^{92}Mo systems present different surface folding potentials in spite of the same nucleon number in the target and projectile. The comparison of the potentials extracted from CC data analyses (Fig. 14 top) and those from double-folding calculations (Fig. 14 bottom) indicates clearly that all our expectations about the isotopic and isotonic dependence of these potentials are reasonably met. A similar result was obtained for the isotopic dependence of the nuclear potential for the $^{16}\text{O} + ^{58,60,62,64}\text{Ni}$ systems, as reported earlier [2]. Nevertheless, the strengths of the “experimental” potentials are

about 40% greater than the folding predictions (see Table 1). Again a similar result was found for the $^{16}\text{O} + ^{58,60,62,64}\text{Ni}$ systems. Possible sources of such discrepancy will be discussed in the next sections. -

Table 1 gives the “diffuseness parameters” (α) obtained from the slopes of the folding potentials, calculated in the surface region by Eq. (7). The folding diffuseness values are similar for all systems and close to the average “experimental” one (0.64 *fm*). A similar result has been obtained for the $^{16}\text{O} + ^{58,60,62,64}\text{Ni}$ systems, and an average value of 0.59 *fm* has been found [1, 2]. These results indicate that the heavy-ion system potentials have a “universal” shape in the surface region rather independent of the “size of the system”. As we will discuss in section 6, the features of the folding potential in the surface interaction region are dependent on the nuclear densities in the nucleus surface region. Since the electron scattering experiments [9] have shown that the heavy nuclei have similar charge diffuseness values, one should expect the potential diffuseness to be similar for different heavy-ion systems.

$$\alpha = \left| \frac{V(R)}{dV/dR} \right| \quad (7)$$

V. Contributions to the Polarization Potential

As discussed in the previous section, a difference of about 40% between the folding potential strengths in the surface interaction region and the corresponding “experimental” values from CC data analysis was found for the $^{16}\text{O} + ^{88}\text{Sr}, ^{90,92}\text{Zr}, ^{92}\text{Mo}$ systems (present work), and also for the $^{16}\text{O} + ^{58,60,62,64}\text{Ni}$ systems (Refs. [1, 2]). We have performed the following studies in order to explain this discrepancy: i) in this section, we intend to investigate how much of such difference is connected to contributions to the polarization potential arising from couplings of reaction channels with negligible cross sections, which were not included in our CC calculations at low energies; ii) in the next section, we will discuss the effects on the folding potential associated with different models assumed for the nuclear matter densities.

Referring back to the $^{16}\text{O} + \text{Ni}$ studies, an extensive and rather com-

plete coupled channel calculation, that included both inelastic excitation and transfer processes, was performed by Keeley et al. [11] for the $^{16}\text{O} + ^{58,62}\text{Ni}$ systems, and an “average” polarization potential was extracted through the solution of the coupled equations. Table 2 contains some results extracted from that work for the $^{16}\text{O} + ^{58}\text{Ni}$ system at $E_{CM} = 28 \text{ MeV}$, since this energy is in the energy range in which we have extracted the “experimental” nuclear potential for that system [2]. We point out the following features of the CC calculations: i) the contribution of the coupling for the $^{16}\text{O} 3^-$ state (which has a large phonon amplitude) is about 50% of the full polarization potential (which corresponds to all coupled channels); ii) the polarization potential due to this 3^- state is about 8% of the folding potential independent of the interaction distance considered. These results indicate that the polarization potential should not change significantly the shape (diffuseness) of the total (folding + polarization) potential in comparison to the folding potential. Another important point is that the strength of the full polarization potential is only about 17% in comparison to the folding potential. This result indicates that the polarization potential should be responsible for less than half of the observed discrepancy (40%) between the “experimental” and the folding potential strengths found in our previous work [2]. In principle, as discussed by Keeley et al. [11], the source of that discrepancy could be other possible couplings such as that for the $^{16}\text{O} 3_1^-$ state. Nevertheless, recent comparison [12] between the predicted fusion cross sections of this full CC analysis and precise fusion data for the $^{16}\text{O} + ^{58,62}\text{Ni}$ systems indicate that such CC calculations overpredict the data at energies below the fusion barrier (see Fig. 3 of Ref. [12]). The inclusion of other reaction channels in the CC calculations certainly would worsen the fusion cross section predictions. Thus, we believe that the strengths of the couplings are not so strong as considered in such calculations and the polarization potential strength should be even less significant in comparison to the bare potential.

We have also performed coupled channel calculations for the $^{16}\text{O} + ^{90}\text{Zr}$ system including the $^{16}\text{O} 3_1^-$ and $^{90}\text{Zr} 3_1^-$ states, besides that for the $^{90}\text{Zr} 2_1^+$ state. For the nuclear potential, we have adopted the “experimental” CC potential according to Table 1. Fig. 15 shows the predicted elastic cross sections for $E_{LAB} = 48 \text{ MeV}$, considering: no couplings (solid line), only the $^{90}\text{Zr} 2_1^+$ coupling (also solid line because the difference is negligible), both couplings $^{90}\text{Zr} 2_1^+ + ^{90}\text{Zr} 3_1^-$ states (dashed line) and $^{90}\text{Zr} 2_1^+ + ^{16}\text{O} 3_1^-$ states (dotted line). The couplings do not have much effect on the elastic scattering

cross sections. In order to fit the data considering the coupling for the $^{16}\text{O } 3_1^-$ state, it is necessary to reduce the “experimental” potential strength by about 7% and the diffuseness parameter persists changeless. These results are very similar to those found for the $^{16}\text{O} + \text{Ni}$ systems. Therefore, we consider that also for the systems studied in the present work, $^{16}\text{O} + ^{88}\text{Sr}, ^{90,92}\text{Zr}, ^{92}\text{Mo}$, the polarization potential is far from being capable of accounting for the detected difference between the folding and the “experimental” potential strengths.

VI. The Missing Potential Strength: Probing the Nuclear Density

As discussed in the previous sections, the ion-ion potentials extracted from low energy CC data analyses are about 40% greater than the theoretical double-folding predictions for the $^{16}\text{O} + ^{58,60,62,64}\text{Ni}, ^{88}\text{Sr}, ^{90,92}\text{Zr}, ^{92}\text{Mo}$ systems, and the polarization potential that arises from couplings to reaction channels with negligible cross sections can only account for part of this difference. We have investigated if the source of such discrepancy is related to the models adopted to describe the ground-state nuclear densities. Since this discrepancy is approximately target independent, we have investigated the projectile density. We have studied which region of the ^{16}O density contributes significantly to the nuclear potential in the surface region. In order to perform such a study, we have taken the ^{90}Zr as the target nucleus and we have included a spline with gaussian shape, according to Eq. (8), on the nuclear density of the ^{16}O nucleus. We have characterized the sensitivity region of the density by varying the position of the perturbation (R_p), and calculating the percentage difference ($100 \times \frac{\Delta V}{V_{\text{unperturbed}}}$) in the strength of the folding potential at the interaction distance $R = 11 \text{ fm}$ ($\Delta V = V_{\text{perturbed}} - V_{\text{unperturbed}}$). The results of such calculations are shown in Fig. 16. The low energy sensitivity region (LESR) for the ^{16}O density lies at radius around 4 fm , a value about 1.3 fm greater the root-mean-square (RMS) radius of the ^{16}O charge distribution [9]. Double-folding calculations show that an increase of about 30% in the ^{16}O density in this surface region (roughly $3 \leq r \leq 5 \text{ fm}$) could explain the theoretical-experimental potential strength discrepancy previously discussed. We point out that nuclear density calculations for the ^{16}O nucleus based on different models give similar density values in the region near the RMS radius, and predict quite different results

in the surface region, which differ from each other by about 30% (see Fig. 17). On the other hand, we have not observed such behavior for the targets studied in this work, as illustrated in Fig. 18.

$$\rho_{perturbed}(r) = \rho_{unperturbed}(r) \left[1 + 0.1e^{-\left(\frac{r-R_p}{0.5}\right)^2} \right] \quad (8)$$

The low energy data analysis for the $^{16}\text{O} + ^{88}\text{Sr}, ^{90,92}\text{Zr}, ^{92}\text{Mo}$ systems have shown that the elastic scattering cross sections are sensitive to an interaction distance region around 11 fm , which corresponds to a region of sensitivity for the nuclear densities about 1.5 fm larger than the RMS radius. For much higher energies, inner distances are probed by elastic scattering cross section data analysis. Such measurements have been performed for the $^{16}\text{O} + ^{90}\text{Zr}$ system at $E_{LAB} = 1503 \text{ MeV}$ [15]. In this case, the elastic scattering cross sections are sensitive to the nuclear potential in an interaction distance region around 8 fm [15], and our analysis indicate that the corresponding density sensitivity region is near the RMS radius. At such high energies and such internal interaction distance region, as discussed in Refs. [16, 17], the polarization potential from reaction channel couplings (Feshbach nonlocality) contributes mainly to the imaginary part of the optical potential, while the effects of nucleon exchange (Pauli nonlocality) are important to the real part of the nuclear interaction. Recently, a model [16]-[18] that takes into account the Pauli non-local nature of the nuclear interaction was developed with the aim to describe the nucleus-nucleus collision at low and high energies. The model is based on the Perey and Buck prescription [19], with the non-local parameter range (b) given by the Jackson and Johnson theoretical prediction [20], $b = b_0 \frac{\mu_0}{\mu}$ ($b_0 = 0.85 \text{ fm}$, μ_0 is the nucleon mass and μ is the reduced mass of the system). In the model, the parameter free non-local real nucleus-nucleus interaction is expressed by

$$V(\vec{R}, \vec{R}') = V_{folding} \left(\frac{R + R'}{2} \right) \frac{1}{\pi^{3/2} b^3} e^{-\left(\frac{\vec{R} - \vec{R}'}{b}\right)^2}, \quad (9)$$

and the corresponding energy-dependent local equivalent potential is expressed approximately by

$$V_{LE}(R, E) \simeq \frac{1 - \sqrt{1 - 4\gamma V_{folding}(R) e^{-\gamma[E - V_C(R)]}}}{2\gamma}, \quad (10)$$

where $\gamma = \mu b^2 / 2\hbar^2$.

For an interaction radius near the barrier radius and energies close to the Coulomb barrier, the local equivalent potential is quite close to the folding one, $V_{LE}(R \simeq R_B, E \simeq V_B) \simeq V_{folding}(R)$, and the effect of the nonlocality is negligible. Fig. 19 shows the folding potential (dashed line) and the local equivalent potential at $E_{LAB} = 1503 \text{ MeV}$ (solid line) for the $^{16}\text{O} + ^{90}\text{Zr}$ system. In Fig. 20, the elastic cross section data [15] for the same system and energy are shown. Also the corresponding optical model predictions, either considering the folding potential (dashed line) or the local equivalent potential (solid line), are shown in the same figure. In the data fit procedure, as reported in Ref. [17], only the Woods-Saxon imaginary potential parameters were allowed to vary. The elastic scattering cross section predictions are quite similar considering any density model of Fig. 17 for the ^{16}O nucleus. The parameter free local equivalent real potential provides a good data prediction (see Fig. 20) without any normalization of the folding potential included in Eq. (10). This result should be compared to the required normalization of 40% in elastic scattering data fits at sub-barrier energies. We again point out that the density sensitivity regions probed at low and high energies are rather different. We stress that different models usually give similar density results in the region close to the RMS radius, and very different density values in the surface region (LESR). Therefore, the low energy elastic scattering data provide a test for different density models which give similar high energy data fits.

VII. Summary and Conclusions

In summary, we have performed coupled channel analysis of elastic and inelastic angular distributions for the $^{16}\text{O} + ^{88}\text{Sr}, ^{90,92}\text{Zr}, ^{92}\text{Mo}$ systems at the sub-barrier energies $43 \leq E_{LAB} \leq 49 \text{ MeV}$. The data are well reproduced with energy-independent nuclear bare potentials, which are real and have an exponential shape in the surface region. These CC potentials have the same diffuseness parameter, $\bar{a} = 0.64 \text{ fm}$, defined within an accuracy of 5% for all systems. The slope of the resulting CC potentials is well reproduced by the

M3Y double-folding calculations using shell model densities for the targets. The isotonic and isotopic dependence of the CC potentials are also reasonably described by the double-folding potential. Very similar results had already been obtained for the $^{16}\text{O} + ^{58,60,62,64}\text{Ni}$ systems. All these results are closely related to the nuclear density features of the collision partners.

Nevertheless, for both sets of systems the strengths of the sub-barrier CC bare potentials are about 40% greater than the corresponding values from M3Y folding potential calculations. Based on a previous extensive and rather complete coupled channel analysis for the $^{16}\text{O} + ^{58,62}\text{Ni}$ systems, we have concluded that the contributions to the polarization potential associated to other reaction channel couplings only account for part of such discrepancy. Our studies indicate that the discrepancy is connected mainly to the ^{16}O nuclear density model adopted in the folding calculations. The predictions of the low energy elastic scattering cross section are very sensitive to the nuclear matter densities in the surface region. In the high energy case, in which the effects on the nuclear interaction due to the non-local nucleon exchange are very important, the sensitivity region for the densities is somewhat more internal than the corresponding region for the sub-barrier case. Thus, a consistent low and high energy elastic scattering data analysis has been demonstrated to be a powerful tool to probe ground-state nuclear densities.

This work was partially supported by Financiadora de Estudos e Projetos (FINEP), Fundação de Amparo à Pesquisa do Estado de São Paulo (FAPESP), Conselho Nacional de Desenvolvimento Científico e Tecnológico (CNPq), and Programa PICD/CAPES da Universidade Federal de Mato Grosso.

We thank Prof. B. A. Brown from Michigan State University, for providing us the computer shell-model codes.

References

- [1] L.C. Chamon, D. Pereira, E.S. Rossi Jr., C.P. Silva, R. Lichtenthaler Filho and L. C. Gomes, Nucl. Phys. **A582** (1995) 305.
- [2] L.C. Chamon, D. Pereira, E.S. Rossi Jr., C.P. Silva, H. Dias, L. Losano and C. A. P. Ceneviva, Nucl. Phys. **A597** (1996) 253.

- [3] N. Anantaraman, Phys. Rev. **C8** (1973) 2245.
- [4] M. Benjelloun, W. Galster and J. Vervier, Nucl. Phys. **A560** (1993) 145.
- [5] T. Tamura, Rev. Mod. Phys. **37** (1965) 679.
- [6] S. Raman, C. H. Malarkey, W. T. Milner, C. W. Nestor Jr. and P. H. Stelson, At. Data Nucl. Data Tables **36** (1987) 1.
- [7] H. Esbensen and F. Videbaek, Phys. Rev. **C40** (1989) 126.
- [8] B. J. Lund, N. P. T. Bateman, S. Utku, D. J. Horen and G. R. Satchler, Phys. Rev. **C51** (1995) 635.
- [9] C. M. De Jager, H. De Vries and C. De Vries, At. Data Nucl. Data Tables **14** (1974) 479.
- [10] G. R. Satchler and W. G. Love, Phys. Rep. **55** (1979) 183.
- [11] N. Keeley, J. S. Lilley and J. A. Christley, Nucl. Phys. **A603** (1996) 97.
- [12] N. Keeley, J. S. Lilley, J. X. Wei, M. Dasgupta, D. J. Hinde, J. R. Leigh, J. C. Mein, C. R. Morton, H. Timmers and N. Rowley, Nucl. Phys. **A628** (1998) 1.
- [13] G. R. Satchler, Nucl. Phys. **A329** (1979) 233.
- [14] M. El-Azab Farid and G. R. Satchler, Nucl. Phys. **A438** (1985) 525.
- [15] P. Roussel-Chomaz, N. Alamanos, F. Auder, J. Barrete, B. Berthier, B. Fernandez and L. Papineau, Nucl. Phys. **A477** (1988) 345.
- [16] M. A. C. Ribeiro, L. C. Chamon, D. Pereira, M. S. Hussein and D. Galetti, Phys. Rev. Lett. **78** (1997) 3270.
- [17] L. C. Chamon, D. Pereira, M. S. Hussein, M. A. C. Ribeiro and D. Galetti, Phys. Rev. Lett. **79** (1997) 5218.
- [18] L. C. Chamon, D. Pereira and M. S. Hussein, Phys. Rev. **C58** (1998) 576.
- [19] F. Perey and B. Buck, Nucl. Phys. **32** (1962) 253.

[20] D. F. Jackson and R. C. Johnson, Phys. Lett. **B49** (1974) 249.

[21] J. W. Negele, Phys. Rev. **C4** (1970) 1260.

FIGURE CAPTIONS

Figure 1. Energy spectrum for the $^{16}\text{O} + ^{92}\text{Mo}$ system at $E_{Lab} = 49 \text{ MeV}$ and $\theta_{Lab} = 160^\circ$. The molybdenum isotopes ^{94}Mo , ^{95}Mo , ^{96}Mo , ^{97}Mo and ^{100}Mo are the main contaminants in the ^{92}Mo target.

Figure 2. Elastic scattering angular distributions for the $^{16}\text{O} + ^{88}\text{Sr}$ system at the bombarding energies $E_{Lab} = 43, 44$ and 45 MeV . The solid lines correspond to coupled channel calculations (see details in the text).

Figure 3. The same as in Fig. 2, for the $^{16}\text{O} + ^{90}\text{Zr}$ system at $E_{Lab} = 46, 47$ and 48 MeV .

Figure 4. The same as in Fig. 2, for the $^{16}\text{O} + ^{92}\text{Zr}$ system at $E_{Lab} = 45, 46, 47$ and 48 MeV .

Figure 5. The same as in Fig. 2, for the $^{16}\text{O} + ^{92}\text{Mo}$ system at $E_{Lab} = 48, 48.5$ and 49 MeV .

Figure 6. The inelastic (2_1^+ target state) angular distributions for the $^{16}\text{O} + ^{90}\text{Zr}$ system at $E_{Lab} = 46, 47$ and 48 MeV . The solid lines in the figure correspond to coupled channel calculations (see text for details).

Figure 7. The same as in Fig. 6, for the $^{16}\text{O} + ^{92}\text{Mo}$ system at $E_{Lab} = 48, 48.5$ and 49 MeV .

Figure 8. Determination of the nuclear real bare potential at the sensitivity radius (R_S) for the $^{16}\text{O} + ^{90}\text{Zr}$, as obtained from CC analysis of the experimental data ($E_{Lab} = 46$ and 48 MeV) considering different values of diffuseness and potential depth parameters.

Figure 9. The nuclear real bare potential as a function of the sensitivity radius for the $^{16}\text{O} + ^{88}\text{Sr}$, $^{90,92}\text{Zr}$ and ^{92}Mo systems. The solid lines in the figure represent the CC potentials with the same diffuseness value ($\bar{a} = 0.64 \text{ fm}$) for all the systems.

Figure 10. Energy level scheme predictions from shell model calculations for the ^{88}Sr , $^{90,92}\text{Zr}$ and ^{92}Mo nuclei. For comparison purpose, the corresponding experimental schemes were included in the figure.

Figure 11. The ground-state proton (dashed lines) and neutron (solid

lines) densities derived from shell model calculations for the ^{88}Sr , ^{90}Zr , ^{92}Zr and ^{92}Mo nuclei.

Figure 12. Proton (dashed line), neutron (solid line), and total (dotted line) double-folding potentials for the $^{16}\text{O} + ^{88}\text{Sr}$, $^{90,92}\text{Zr}$ and ^{92}Mo systems, using shell model densities for the target nuclei and charge distribution shape density (Eq. 2) for the projectile (see text for details).

Figure 13. Comparison between ground-state proton (a) and neutron (b) densities in the surface region, for the ^{88}Sr , ^{90}Zr , ^{92}Zr and ^{92}Mo nuclei.

Figure 14. Comparison between the bare potentials from CC data analyses (top) and double-folding calculations (bottom), for the $^{16}\text{O} + ^{88}\text{Sr}$, $^{90,92}\text{Zr}$ and ^{92}Mo systems (see text for details).

Figure 15. Comparison between the experimental elastic scattering angular distribution for the $^{16}\text{O} + ^{90}\text{Zr}$ system ($E_{Lab} = 48 \text{ MeV}$) and different CC calculations which include: a) no reaction channel (solid line), b) only the ^{90}Zr 2_1^+ state (also solid line), c) the 2_1^+ and 3_1^- states of the ^{90}Zr nucleus (dashed line), and d) the 2_1^+ and 3_1^- states of the ^{90}Zr and ^{16}O nuclei, respectively (dotted line).

Figure 16. a) The charge distribution shape nuclear density for the ^{16}O nucleus (Eq. 2), indicating the “low energy sensitivity region (LESR)” in the determination of the bare potential through sub-barrier elastic data analysis. b) The percentage difference ($100 \times \frac{\Delta V}{V_{unperturbed}}$) in the strength of the folding potential at $R = 11 \text{ fm}$ for the $^{16}\text{O} + ^{90}\text{Zr}$ system (see text for details).

Figure 17. Different ^{16}O nuclear density predictions considering: a) the charge distribution shape of Eq. 2 (solid line), b) shell model calculations from Ref. [14] (dashed line), and c) Hartree-Fock calculations from Ref. [21] (dotted line). In the figure are indicated the root-mean-square radius (RMS), and the “low energy sensitivity region” in the determination of the CC potential (LESR).

Figure 18. Comparison between proton and neutron densities for the ^{90}Zr nucleus considering shell model (this work) and Hartree-Fock (Ref. [21]) calculations. In the figure are indicated the root-mean-square radius (RMS) and the “low energy sensitivity region” in the determination of the CC potential

(LESR).

Figure 19. The local equivalent potential (solid line) for the $^{16}\text{O} + ^{90}\text{Zr}$ system at the bombarding energy $E_{Lab} = 1503 \text{ MeV}$. The dashed line represents the corresponding double-folding potential (Eq. 1).

Figure 20. Optical model elastic scattering data fits for the $^{16}\text{O} + ^{90}\text{Zr}$ system at the bombarding energy $E_{Lab} = 1503 \text{ MeV}$, considering for the nuclear interaction: a) the double-folding potential (dashed line), and b) the local equivalent potential (solid line). In the data fits only the Woods-Saxon imaginary potential parameters were allowed to vary.

TABLES

Table 1: The diffuseness values from CC (a) and double-folding (α) calculations, and also the strengths of the CC (V_{CC}) and double-folding (V_{fold}) potentials at the interaction distance $R = 11$ fm.

nucleus	a (fm)	α (fm)	V_{CC} (MeV)	V_{fold} (MeV)	V_{CC}/V_{fold}
^{88}Sr	0.71 ± 0.05	0.584	0.90 ± 0.03	0.628	1.43 ± 0.05
^{90}Zr	0.63 ± 0.03	0.586	0.97 ± 0.02	0.675	1.44 ± 0.03
^{92}Zr	0.61 ± 0.05	0.607	1.20 ± 0.04	0.787	1.52 ± 0.05
^{92}Mo	0.63 ± 0.06	0.587	0.98 ± 0.02	0.716	1.37 ± 0.03

Table 2: Double-folding potential (V_{fold}) and polarization potential contribution corresponding to the coupling for the ^{16}O 3_1^- state only ($V_{pol}^{3_1^-}$) and also to all reaction channels included in the CC calculations (V_{pol}^{full}), for the $^{16}\text{O} + ^{58}\text{Ni}$ system at $E_{CM} = 28$ MeV. These values were extracted from Refs. [15, 2] at three different surface interaction radii.

R (fm)	$V_{pol}^{3_1^-}$ (MeV)	V_{pol}^{full} (MeV)	V_{fold} (MeV)
10.0	0.08	0.16	0.91
10.5	0.03	—	0.37
11.0	0.006	—	0.064

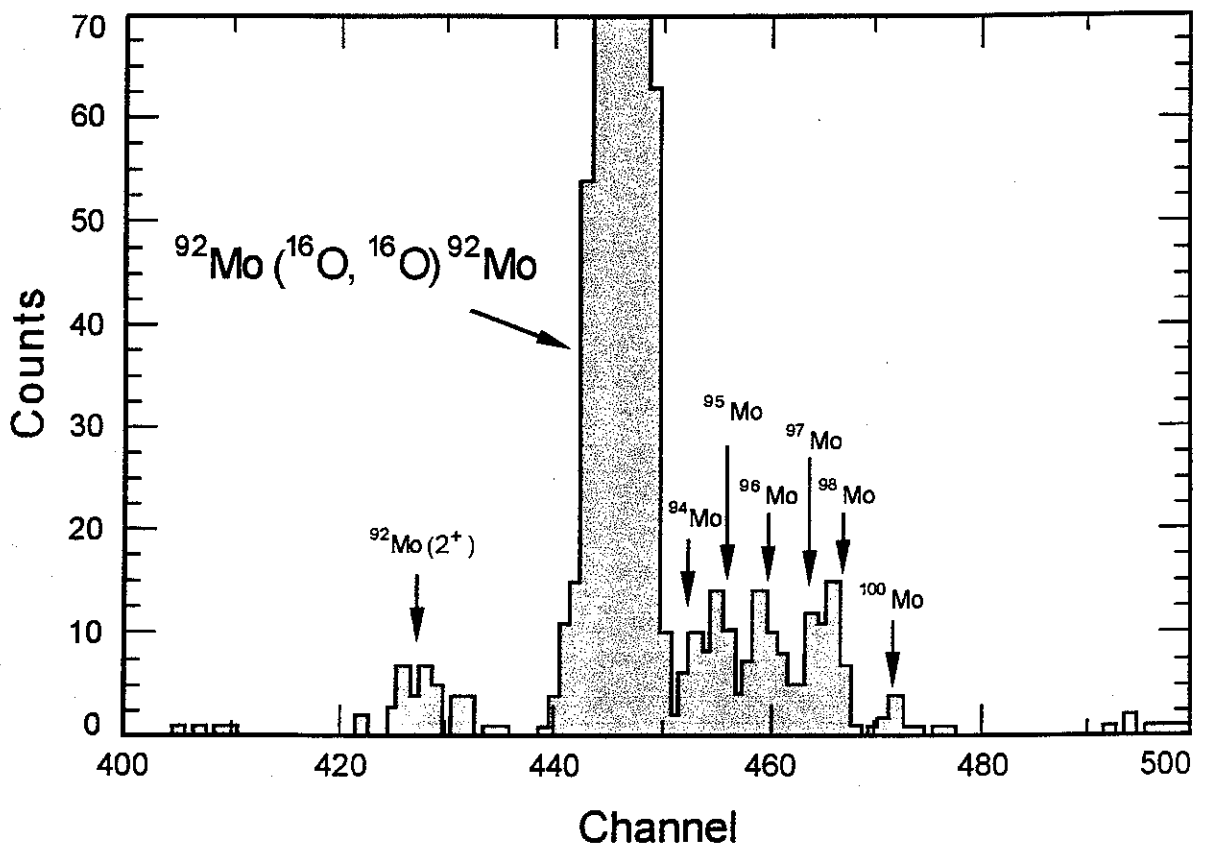


Fig. 1

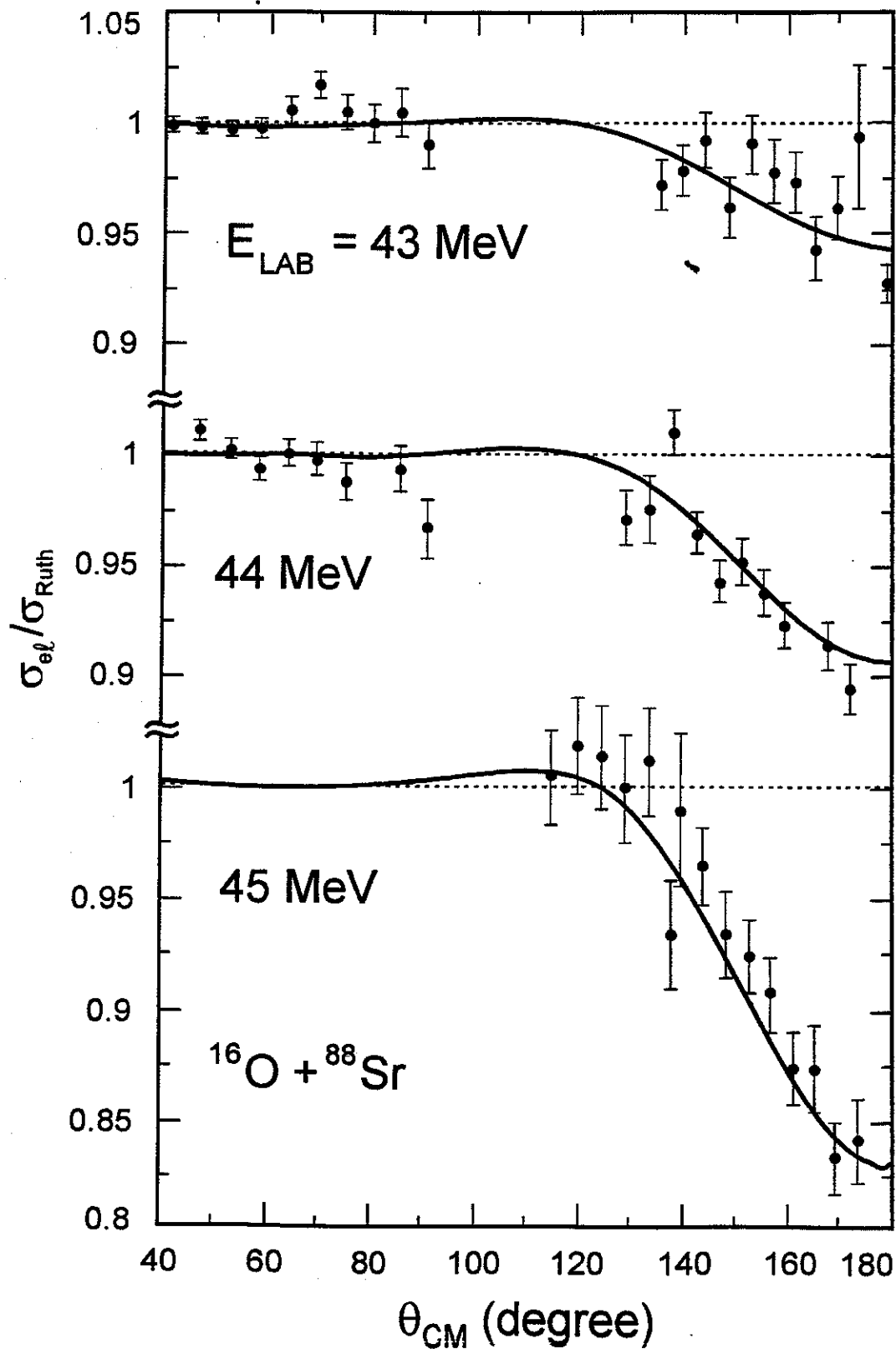


Fig. 2

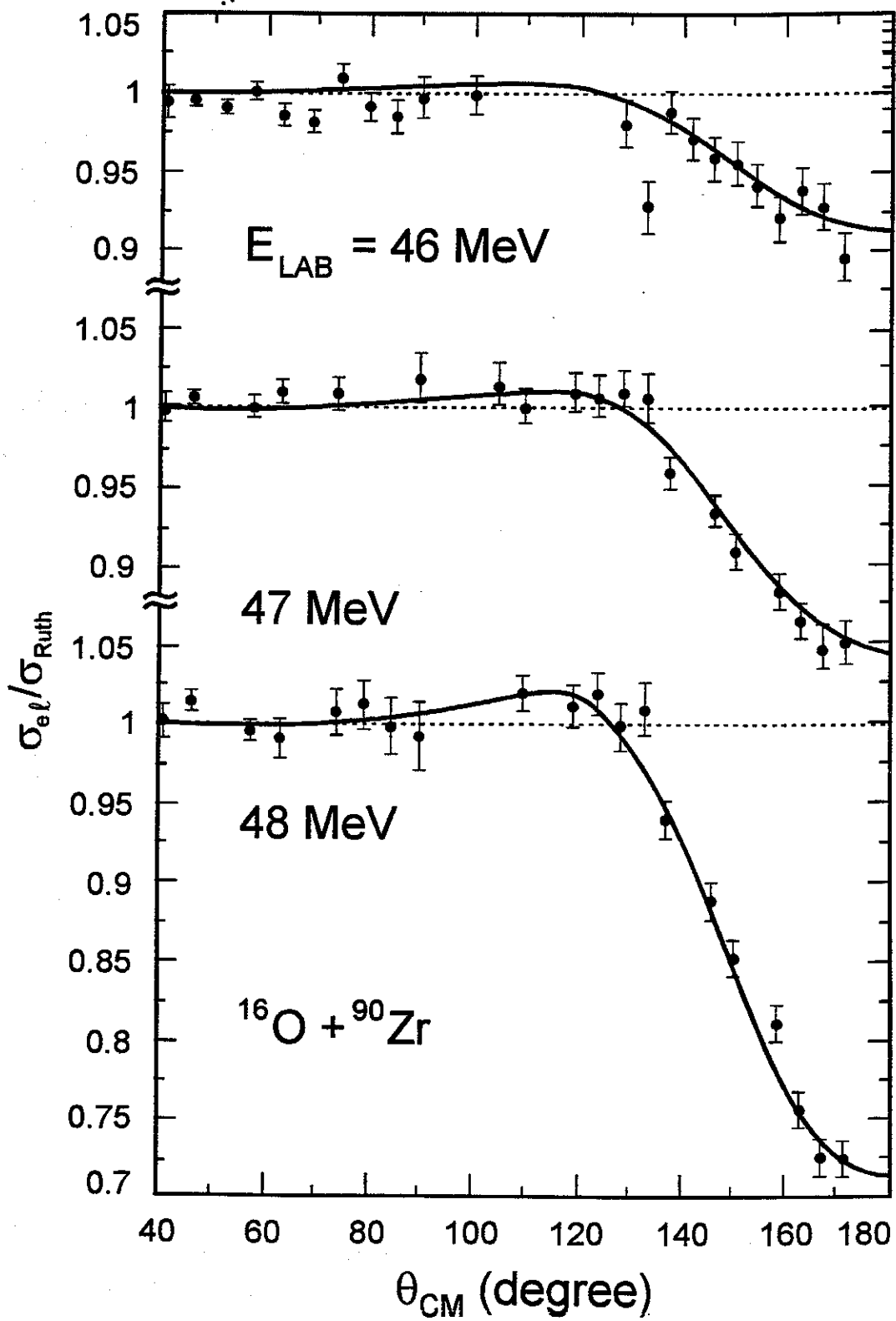


Fig. 3

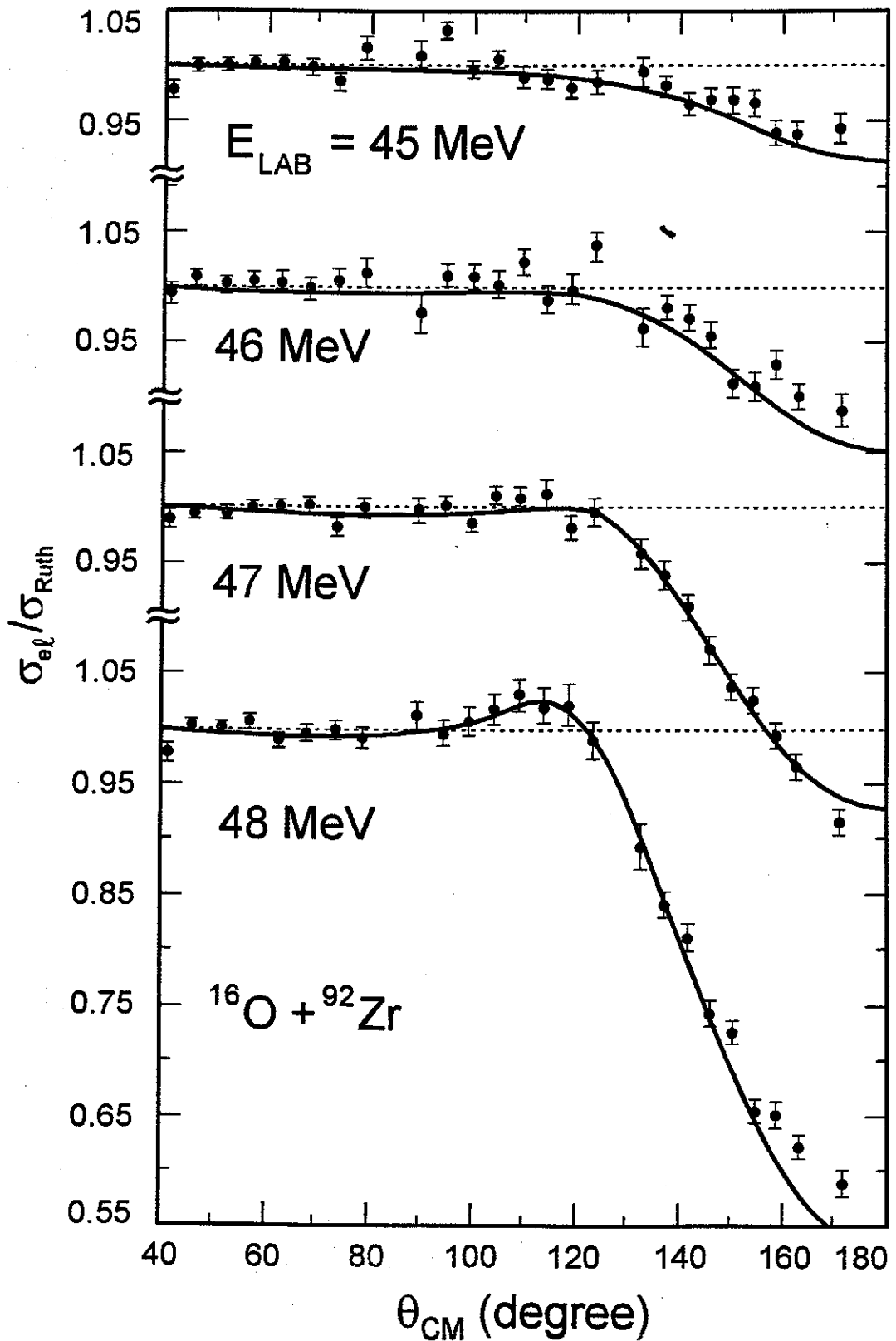


Fig. 4

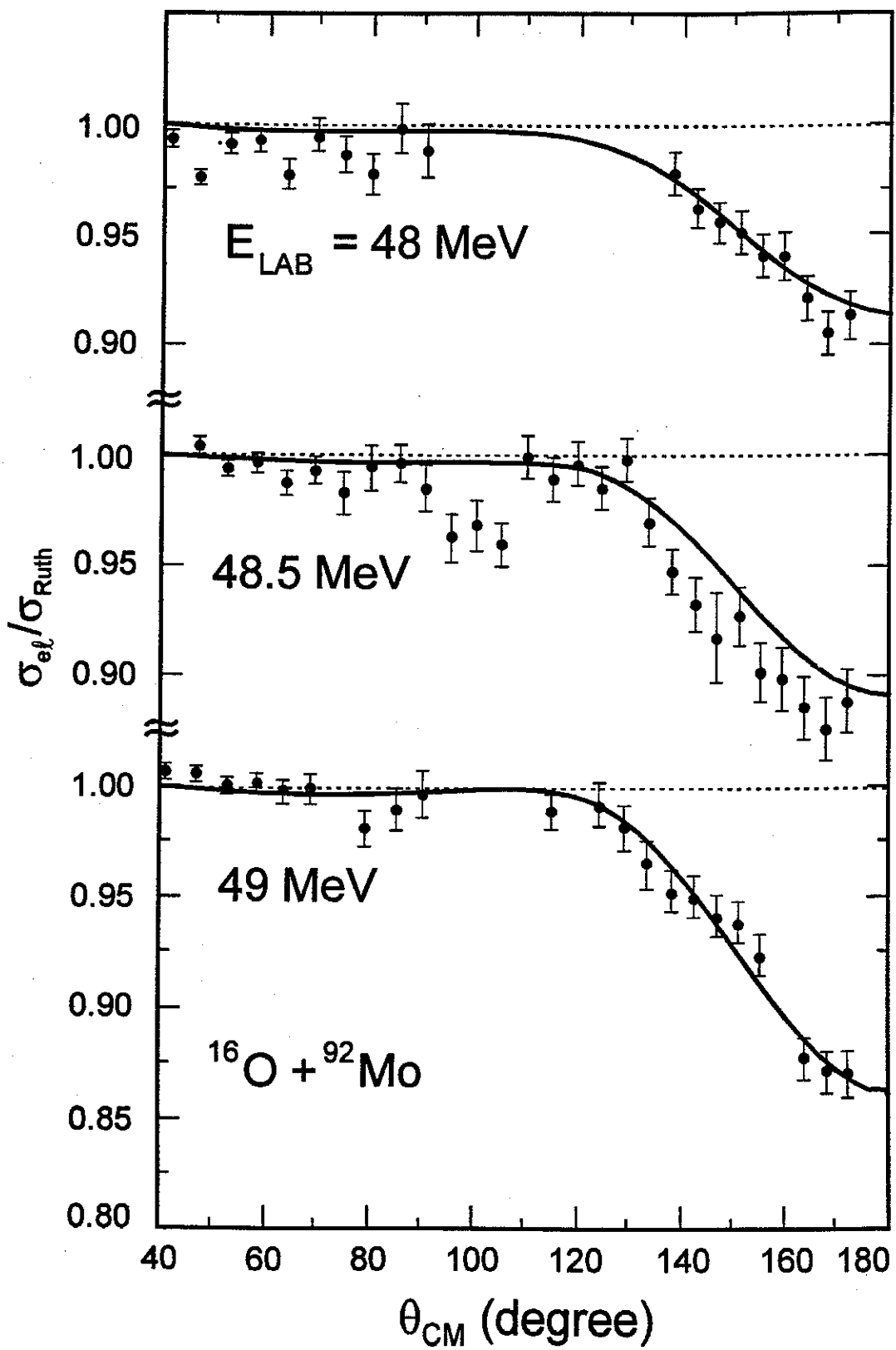


Fig. 5

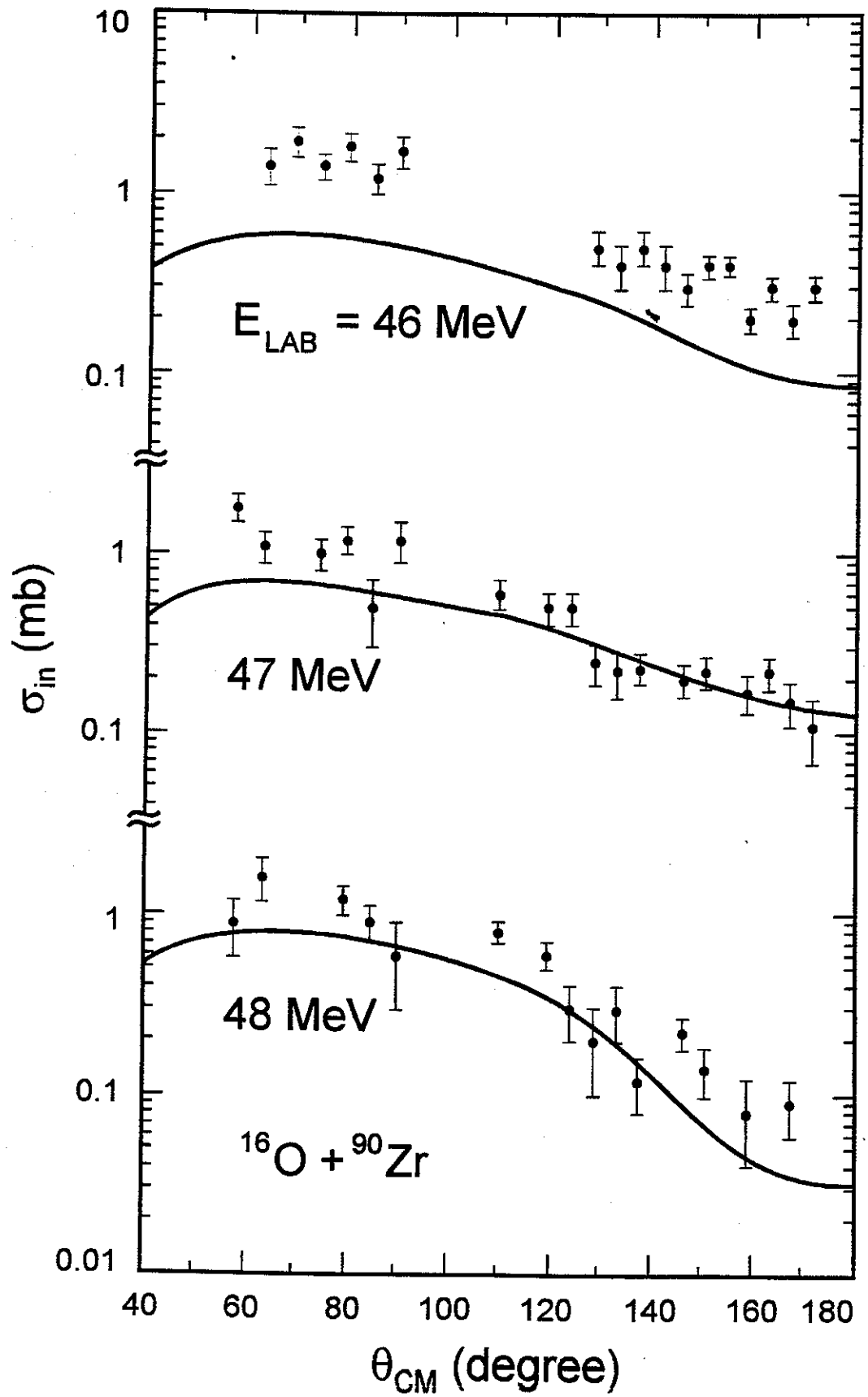


Fig. 6

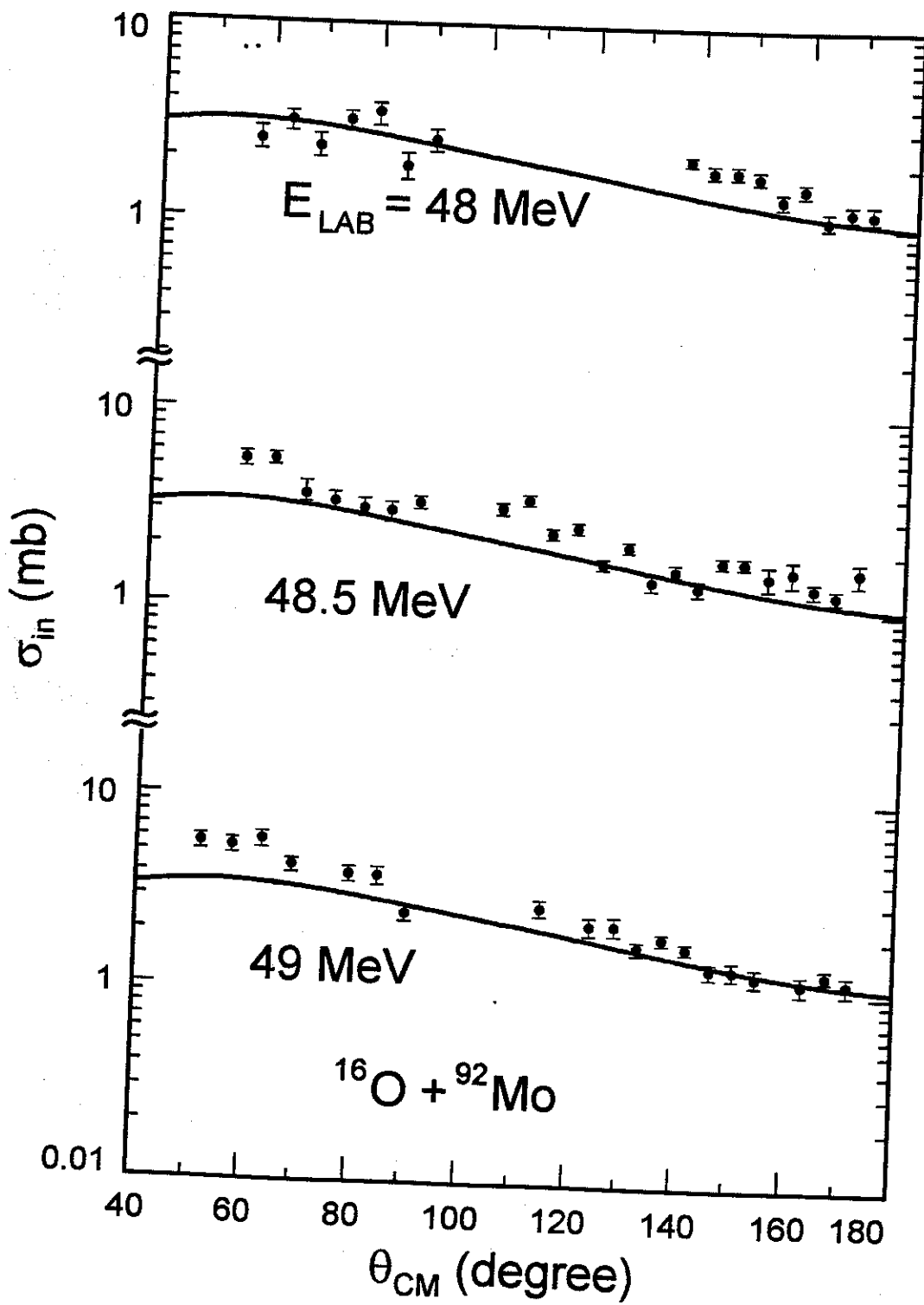


Fig. 7

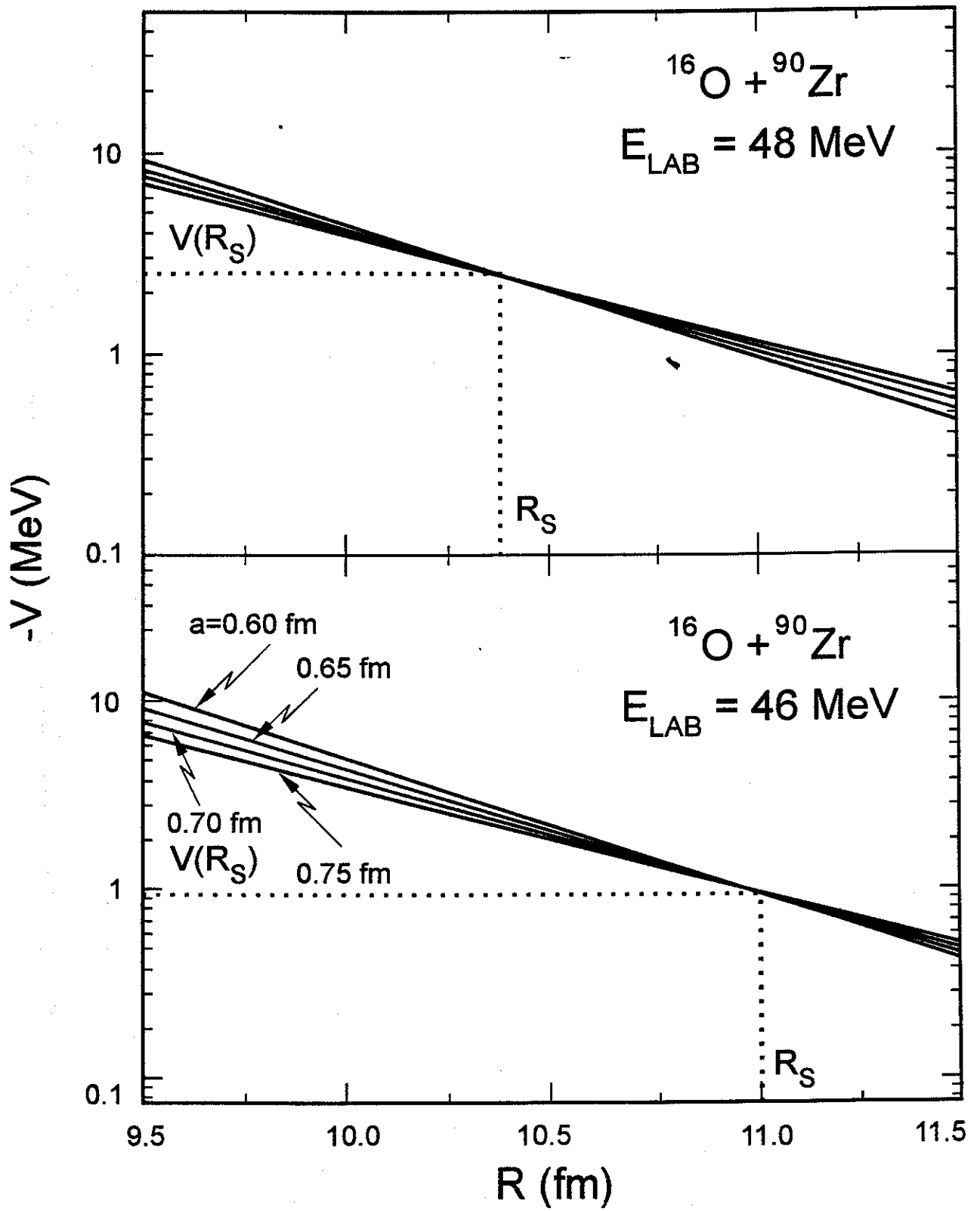
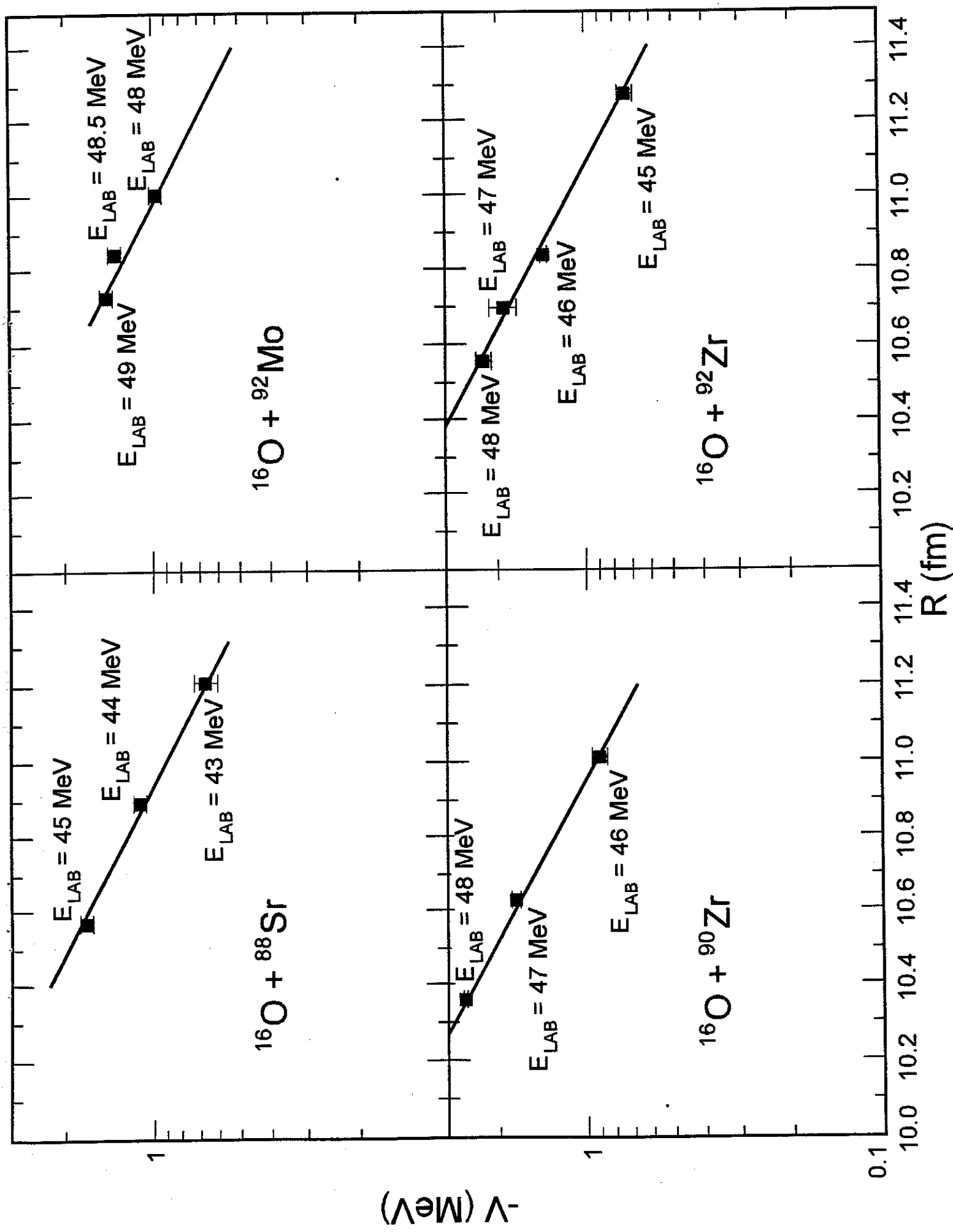
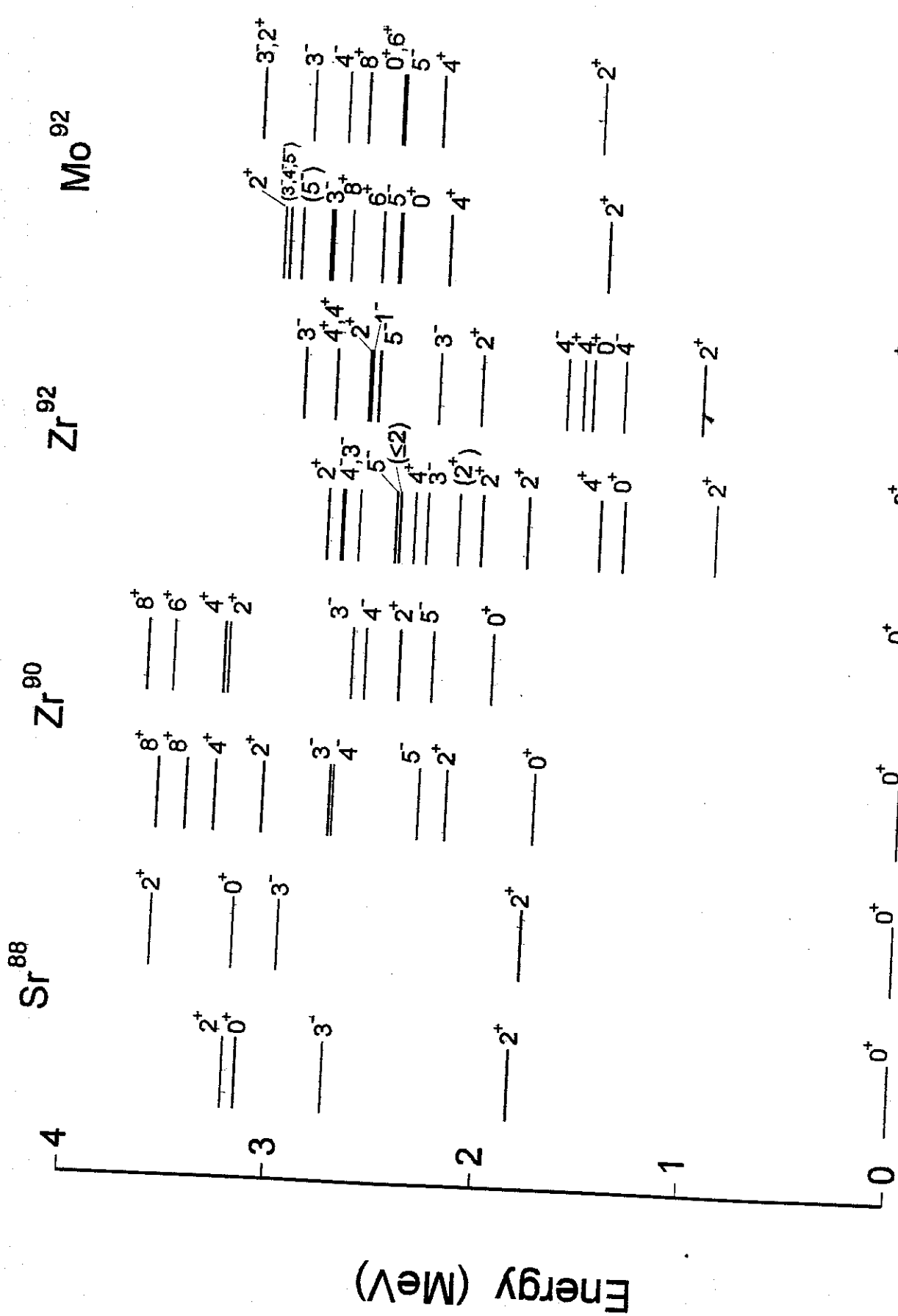


Fig. 8





Exp. Theory Exp. Theory Exp. Theory

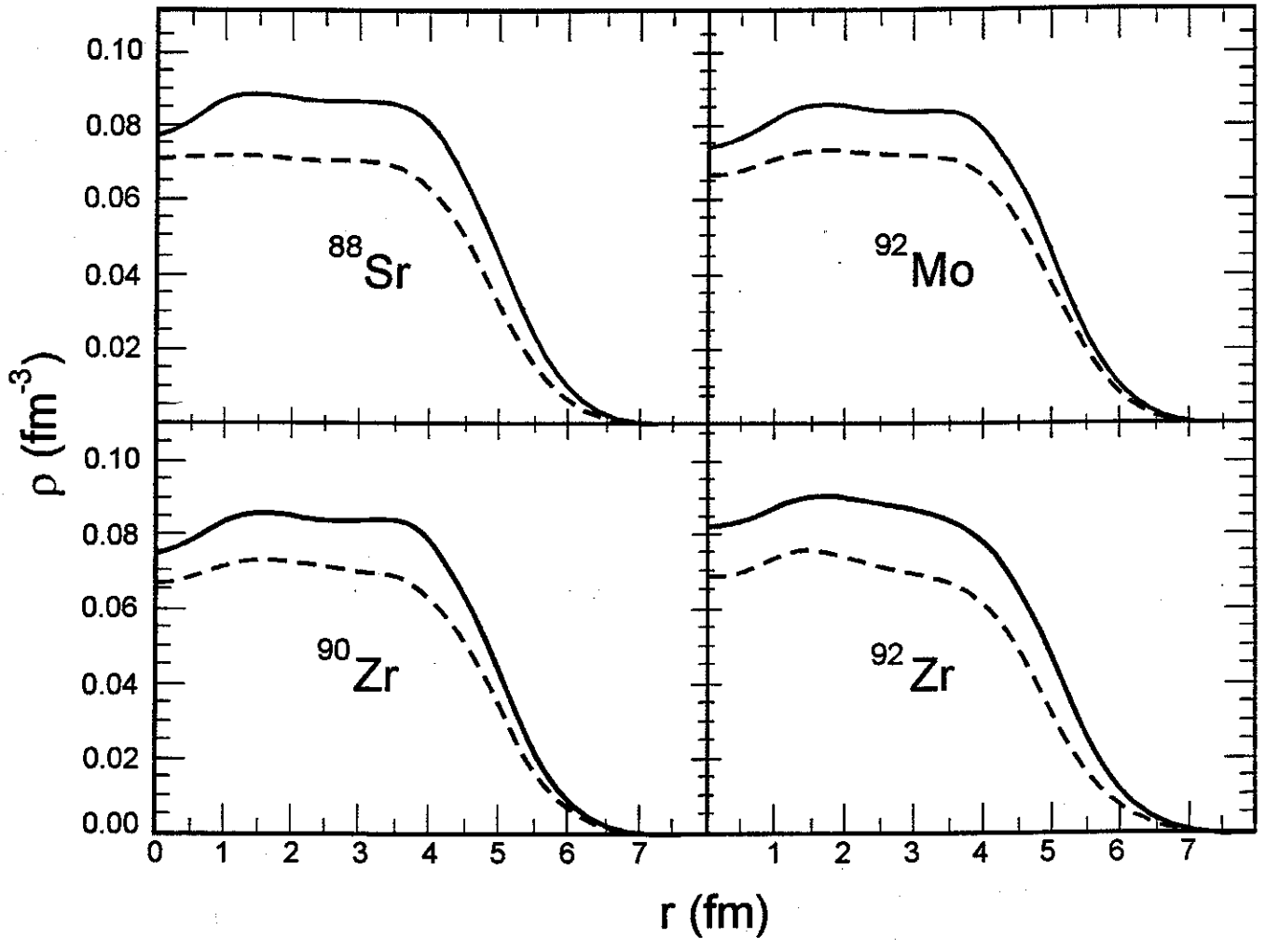


Fig. 11

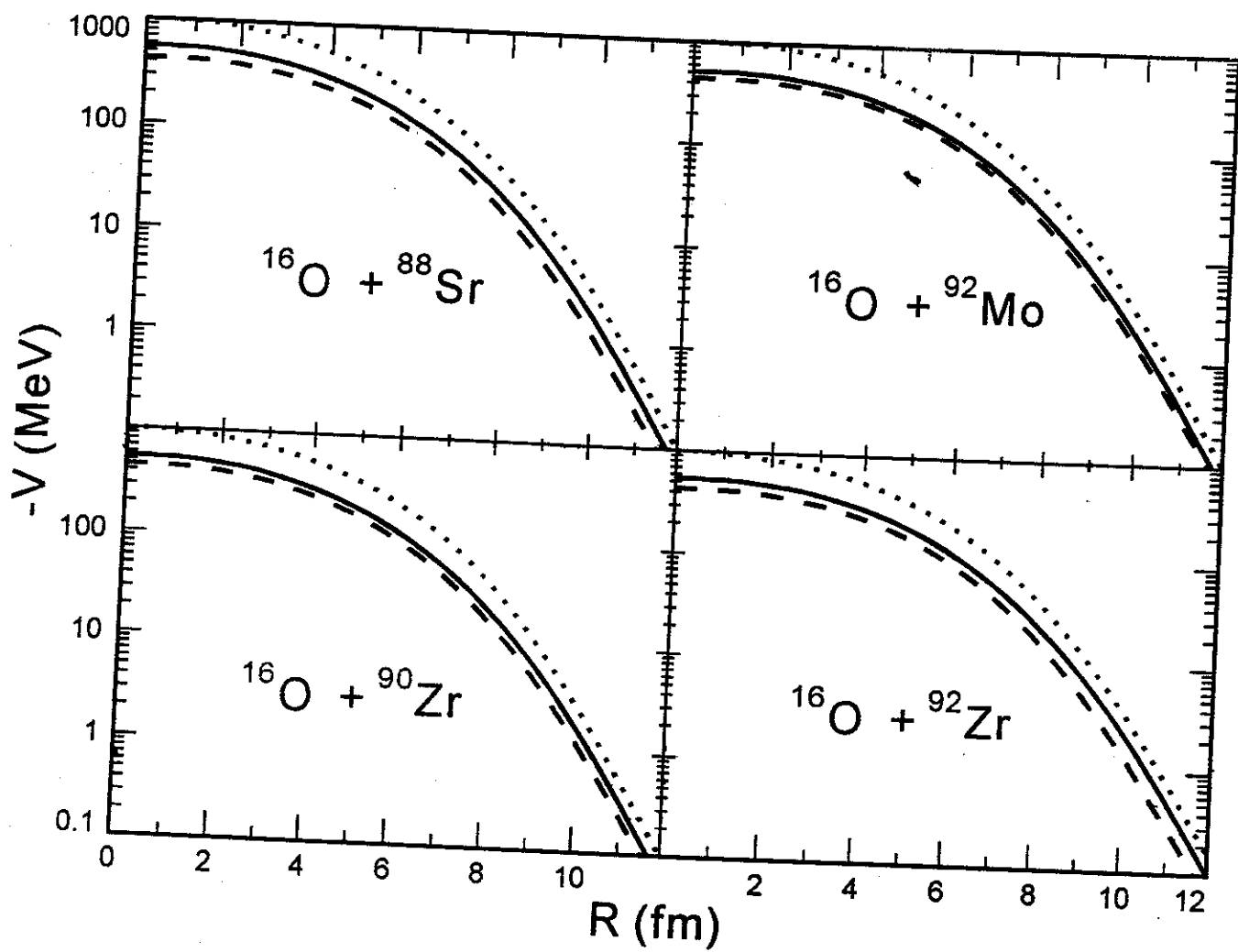


Fig. 12

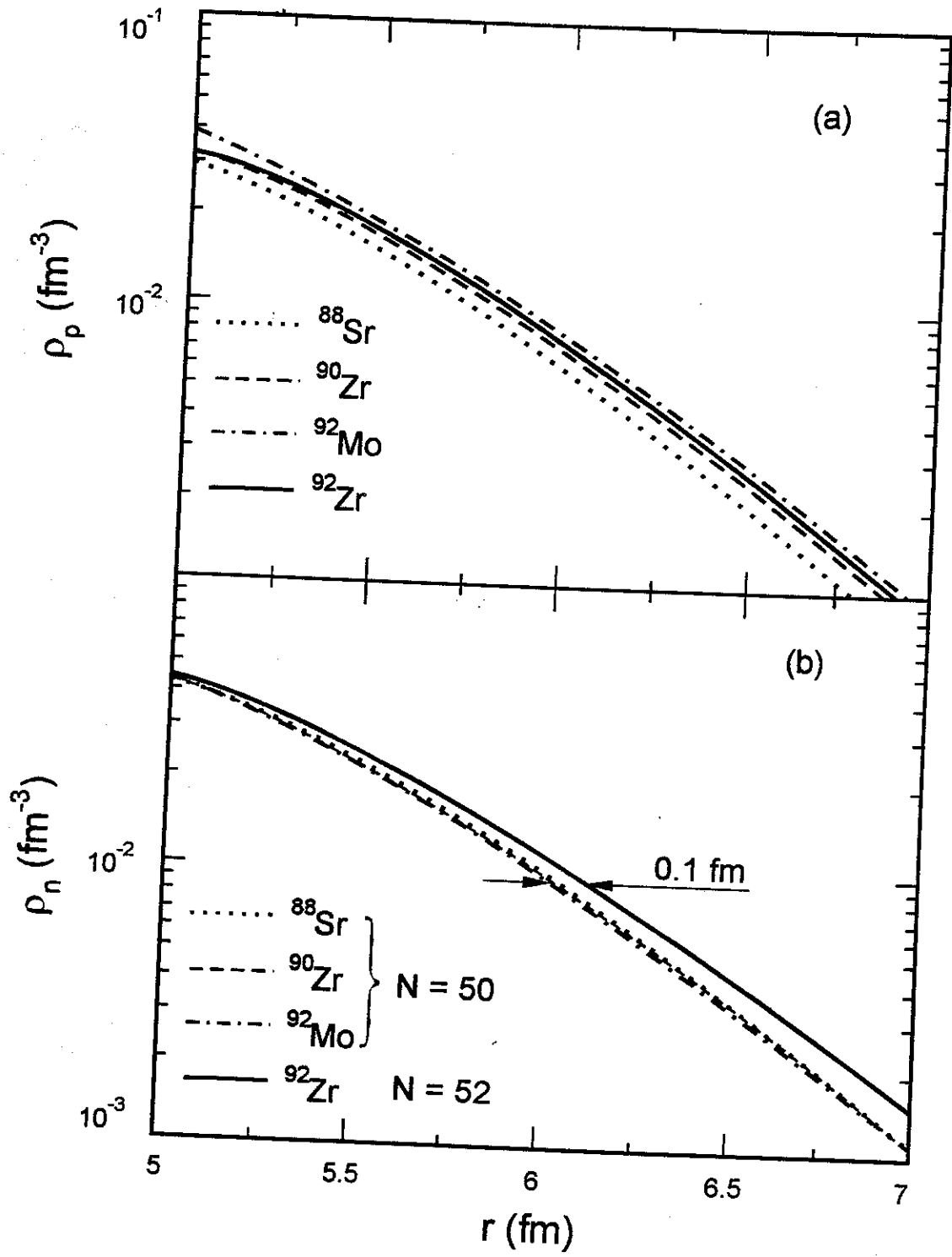


Fig. 13

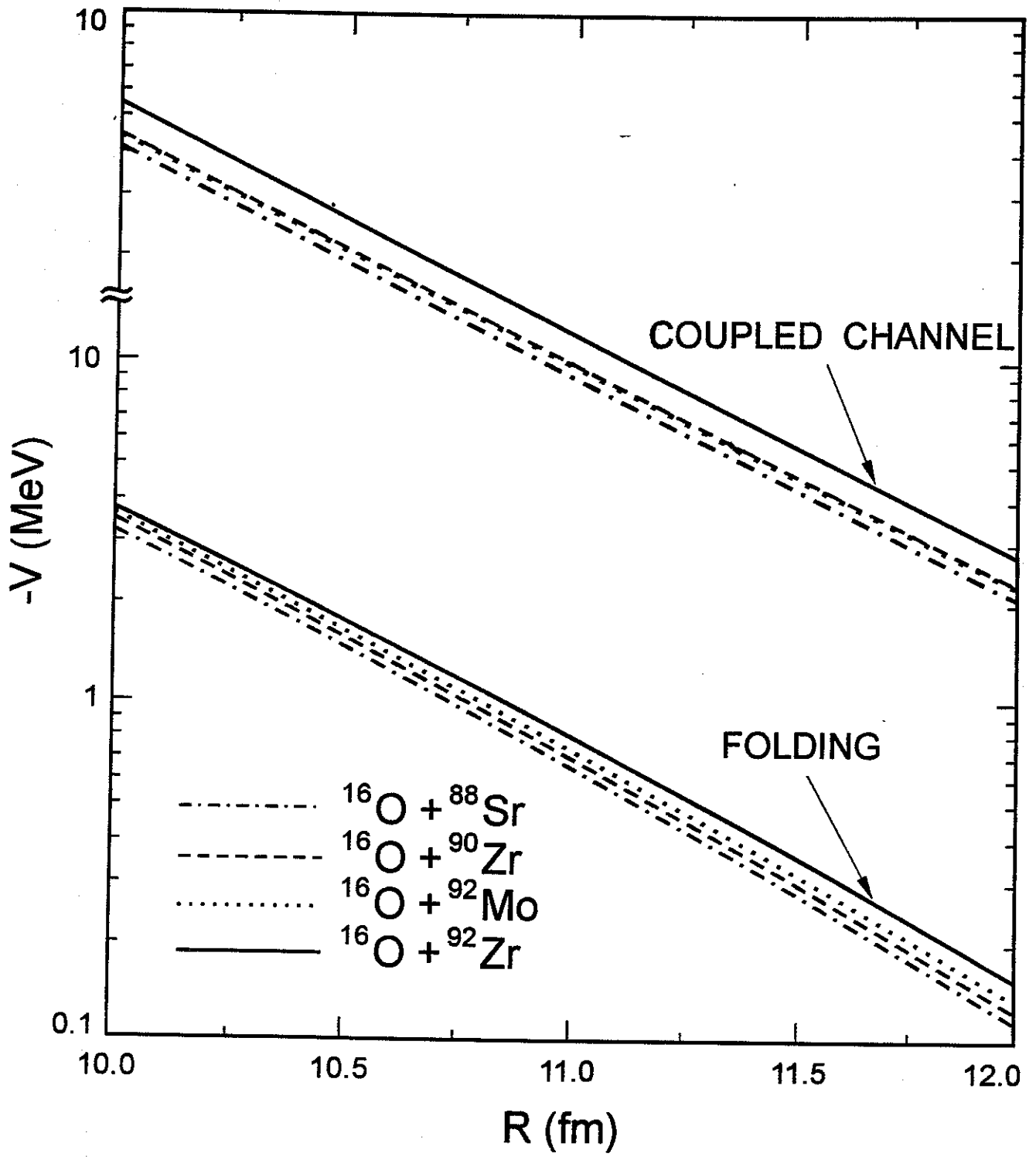


Fig. 14

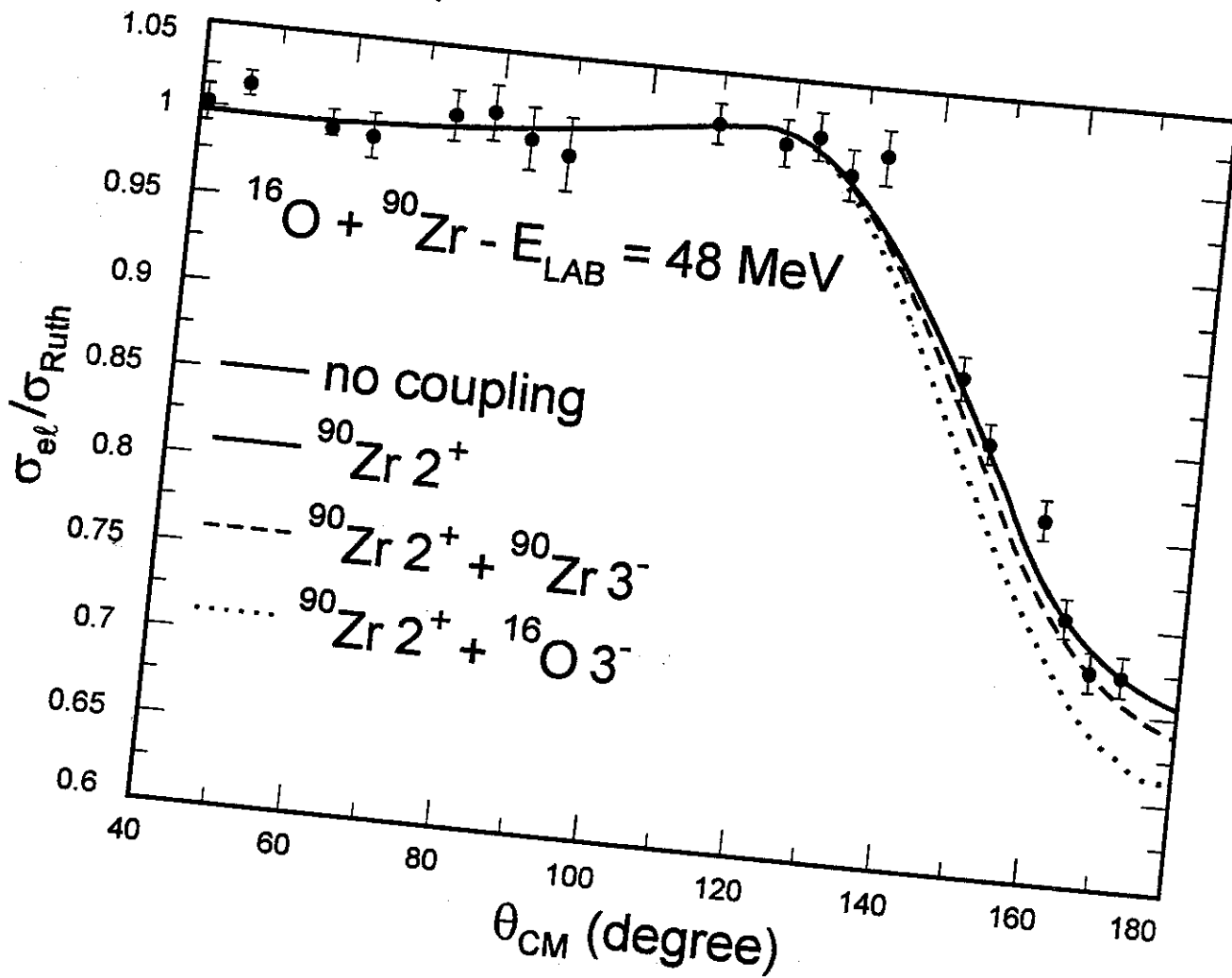


Fig. 15

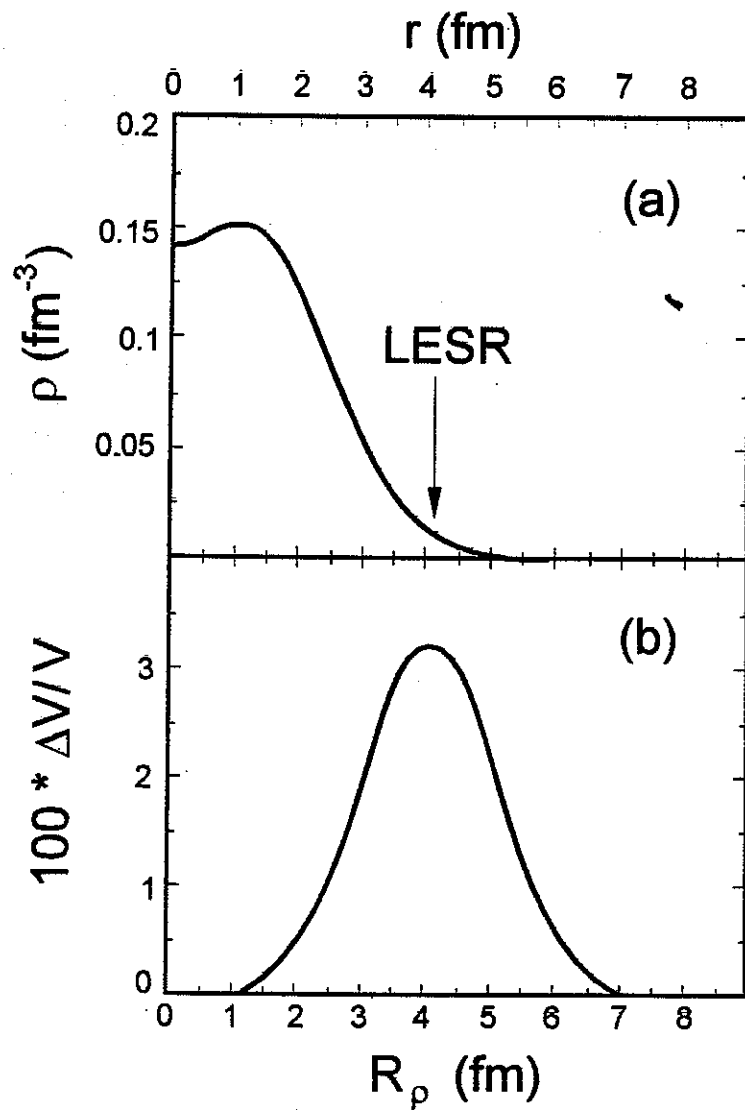


Fig. 16

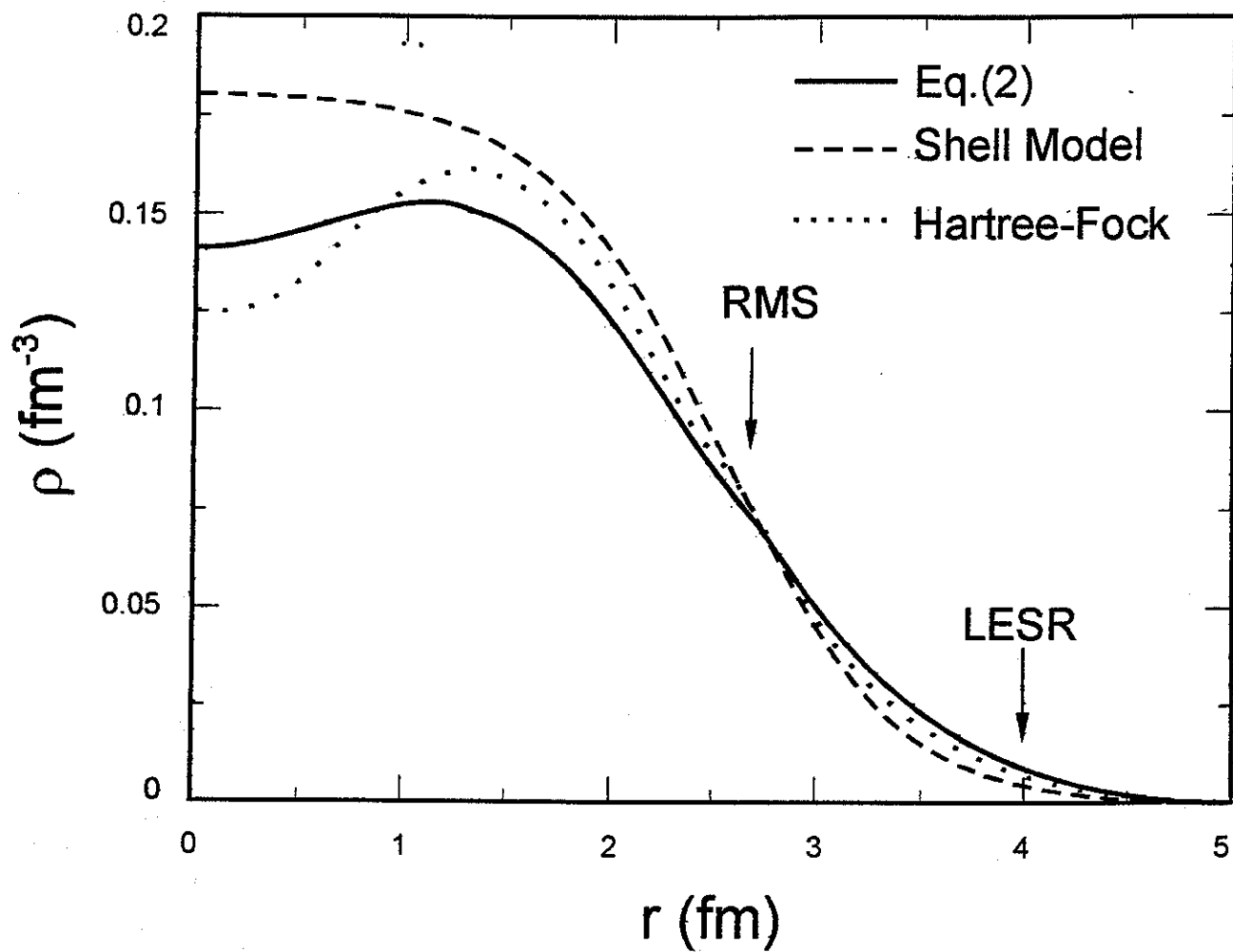


Fig. 17

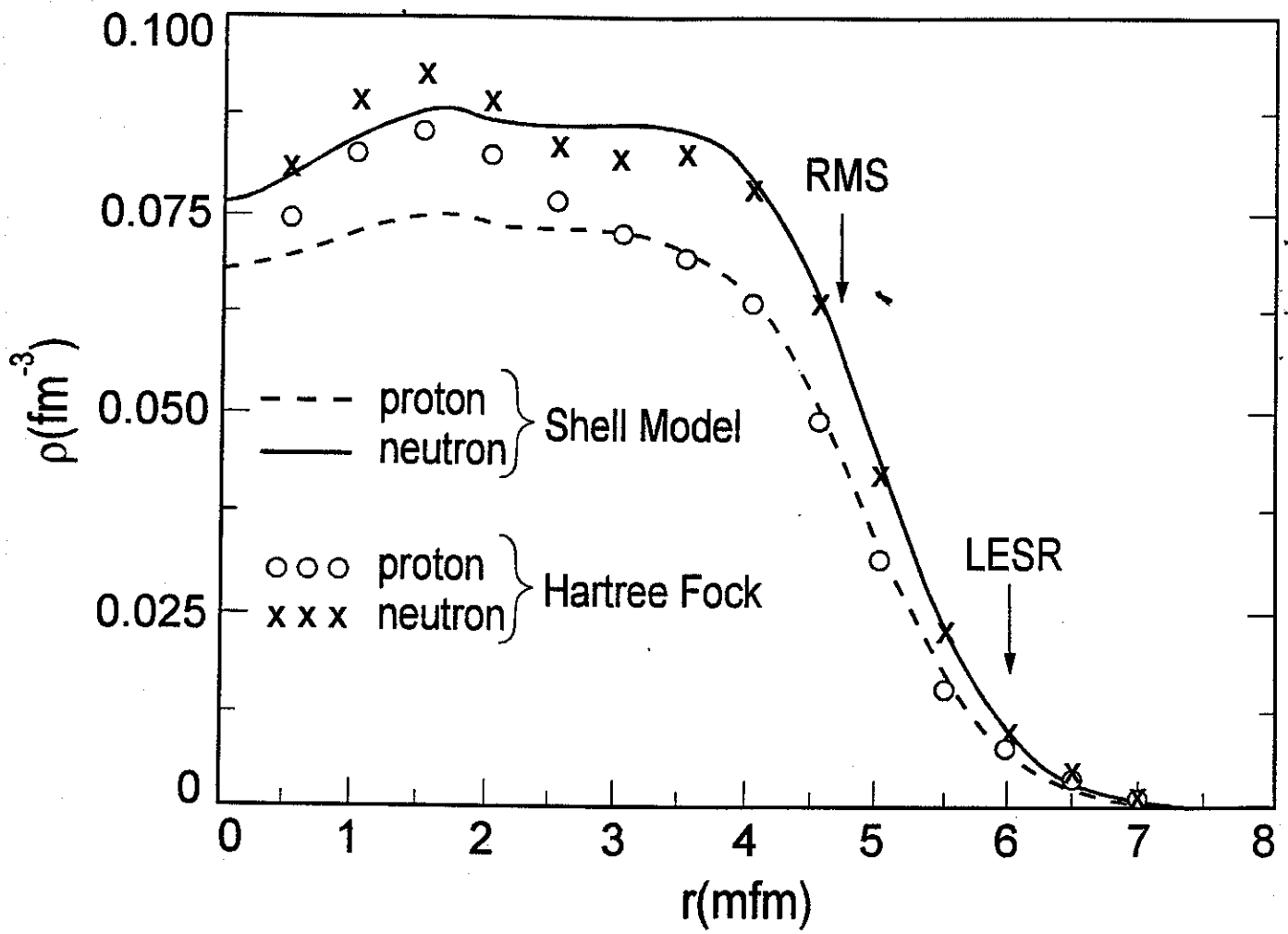


Fig. 18

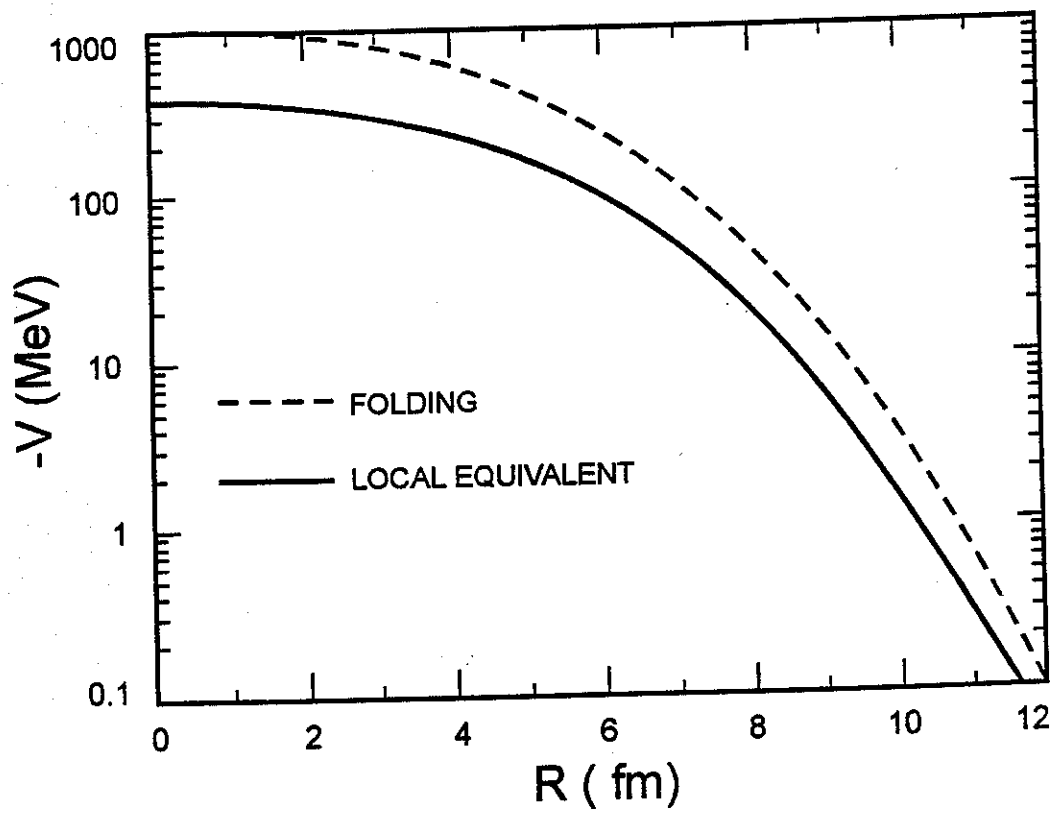


Fig. 19

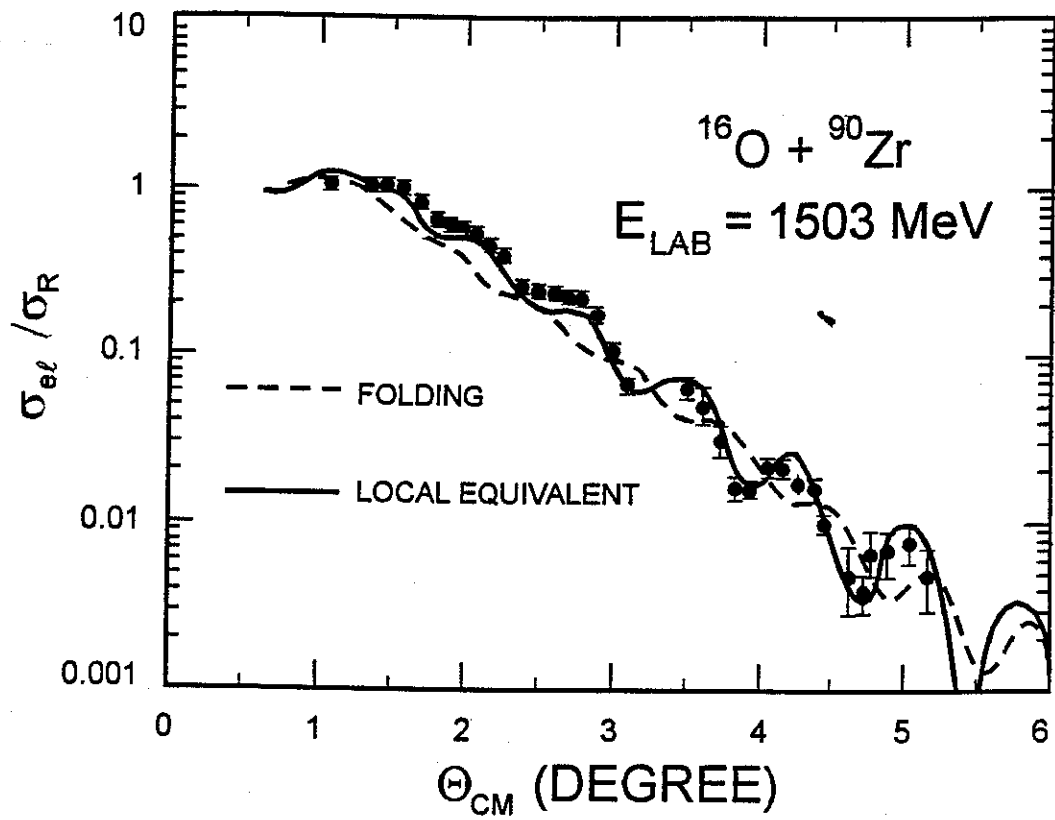


Fig. 20